Biophysical Journal
Article

Biophysical Society

# Negatively charged residues in the membrane ordering activity of SARS-CoV-1 and -2 fusion peptides

Alex L. Lai[1,*] and Jack H. Freed[1,*]
[1]Department of Chemistry and Chemical Biology, Cornell University, Ithaca, New York

ABSTRACT Entry of coronaviruses into host cells is mediated by the viral spike protein. Previously, we identified the bona fide fusion peptides (FPs) for severe acute respiratory syndrome coronavirus ("SARS-1") and severe acute respiratory syndrome coronavirus-2 ("SARS-2") using electron spin resonance spectroscopy. We also found that their FPs induce membrane ordering in a $Ca^{2+}$-dependent fashion. Here we study which negatively charged residues in SARS-1 FP are involved in this binding, to build a topological model and clarify the role of $Ca^{2+}$. Our systematic mutation study on the SARS-1 FP shows that all six negatively charged residues contribute to the FP's membrane ordering activity, with D812 the dominant residue. The corresponding SARS-2 residue D830 plays an equivalent role. We provide a topological model of how the FP binds $Ca^{2+}$ ions: its two segments FP1 and FP2 each bind one $Ca^{2+}$. The binding of $Ca^{2+}$, the folding of FP (both studied by isothermal titration calorimetry experiments), and the ordering activity correlate very well across the mutants, suggesting that the $Ca^{2+}$ helps the folding of FP in membranes to enhance the ordering activity. Using a novel pseudotyped viral particle-liposome methodology, we monitored the membrane ordering induced by the FPs in the whole spike protein in its trimer form in real time. We found that the SARS-1 and SARS-2 pseudotyped viral particles also induce membrane ordering to the extent that separate FPs do, and mutations of the negatively charged residues also significantly suppress the membrane ordering activity. However, the slower kinetics of the FP ordering activity versus that of the pseudotyped viral particle suggest the need for initial trimerization of the FPs.

## INTRODUCTION

Since the outbreak of the ongoing COVID-19 pandemic in Wuhan, China, at the end of 2019, there have been more than 200 million cases and more than 4 million deaths associated with COVID-19. The United States alone has more than 35 million cases and 0.6 million deaths. It has severely harmed our public health, economy, and social life. Even though vaccines have been developed, the rapid evolution of variants still poses a great threat: the delta variant can escape from the protection of most vaccines, and as a result, even fully vaccinated persons can be infected. A better understanding of the mechanism of COVID-19 transmission is among the central agendas to save our society from the pandemic.

The cause of COVID-19 is severe acute respiratory syndrome coronavirus-2 ("SARS-2"), which belongs to the family of coronaviruses (CoVs), a diverse group of enveloped viruses that infect humans and animals, with several recent examples of zoonotic transmission including severe acute respiratory syndrome CoV ("SARS-1") and Middle East respiratory syndrome (MERS) (1), which were responsible for pandemic outbreaks in 2003 (774 deaths) and 2012 (624 deaths), respectively (1). These 3 viruses share many common features, including the mechanism of viral infection.

The viral spike protein (S) is a CoV glycoprotein located on the viral envelope. It is required to mediate viral entry into the host cells and is a major pathogenicity determinant (2,3). The S proteins of SARS-1, SARS-2, and MERS anchor on the viral envelope membrane in the form of trimers. Each monomer consists of S1 and S2 subunits. The 2 major steps in viral entry are (1) receptor binding, in which the S1 subunit recognizes a receptor on the host cell membrane (e.g., ACE2) and attaches the virus to the host cell, followed by (2) membrane fusion, in which the S2 subunit mediates the viral envelope membrane and the host membrane, fusing together and releasing the virion into the host cell. Membrane fusion is a required stage in viral entry (4); thus, blocking the membrane fusion could be an objective leading to vaccines and therapies to combat COVID-19 (5).

*Submitted September 27, 2021, and accepted for publication December 16, 2021.*

*Correspondence: ll564@cornell.edu or jhf3@cornell.edu

Editor: Alemayehu Gorfe.
https://doi.org/10.1016/j.bpj.2021.12.024

The major region of S that interacts with lipid bilayers of the host is called the fusion peptide (FP). Almost all enveloped viruses have a glycoprotein and the corresponding FP, as it is critical for membrane fusion because it inserts into the host lipid bilayer upon activation of the fusion process, perturbing the membrane structure and thereby initiating membrane fusion (6,7). Previously, we used phospholipid spin labels to detect the local perturbation of the membrane by the viral FP and TMD (8–14).

The S proteins and FP of SARS-1, SARS-2, and MERS have several distinct features compared with the other class I viral fusion proteins, including the influenza hemagglutinin (HA) and the HIV envelope protein (Env). First, we note that influenza and HIV Envs are known to be activated by host cell proteases to cleave the proto-glycoproteins into 2 subunits; this occurs at a single, restricted site directly upstream of their FP. By contrast, CoVs typically have two distinct cleavage sites (S1/S2 and S2′), which can be activated by a much wider range of proteases. As a result, we have found that the FP is exposed only after the cleavage event at the S2′ site, and using continuous-wave ESR (Fig. 1 *A*), we have identified that the bona fide FP is directly downstream of the S2′ site for all of SARS-1, SARS-2, and MERS CoV cases (12,15,16) (Fig. 1 *A*). This means that CoVs have unique flexibility in the ability to invade new cell types, tissues, and host species.

Second, and relevant to this study, we found that the viral entry of the CoVs is $Ca^{2+}$ dependent (12,15,16), which is quite rare among enveloped viruses (13). We also found that the function of the CoV FPs is $Ca^{2+}$ dependent, and while the SARS-1 and SARS-2 FPs bind $Ca^{2+}$ at a 1:2 (FP:$Ca^{2+}$) ratio, the MERS FP binds $Ca^{2+}$ at a 1:1 ratio. Thus, we hypothesize that the FP is where the target for the $Ca^{2+}$ is in this $Ca^{2+}$-dependent viral entry mechanism. This is important because the FP domain is largely conserved compared with other parts of the S protein, thus making it an ideal target for vaccines and antiviral drugs. It also raises the possibility of repurposing U.S. Food and Drug Administration-approved drugs in blocking $Ca^{2+}$ channels for COVID-19 treatment. However, how the CoV FPs interact with $Ca^{2+}$ and how this interaction affects the function of the FP and the viral entry remain largely unknown.

There is no crystal structure of intact S, limiting our mechanistic understanding of CoV fusion. While the basic structure of the S of SARS-1 and SARS-2 can be revealed using cryoelectron microscopy techniques (17–20) and part of the SARS-2 S2 subunit has been solved by x-ray crystallography (21,22), many structural and functional aspects remain undetermined. Furthermore, the FP adopts its active conformation only in membranes (12), which is generally not determined in the crystallographic structure, as the FP is relatively hydrophobic and intrinsically disordered. The structure of the SARS-2 FP has been solved only recently, using nuclear magnetic resonance (NMR) in bicelles (23). Still, continuous-wave ESR is a useful technique to study the effect of FPs on membrane structure with implications for the mechanism leading to membrane fusion. It can also be used to determine the peptide structure in the membrane by pulse-dipolar ESR (24,25) and power saturation ESR (26).

We focus primarily on the SARS-1 FP-$Ca^{2+}$ interaction and its effect on membranes, using mainly continuous-wave ESR. But we also include SARS-2 in this study. We attempt to answer four questions: First, as there are six negatively charged residues on the FP, which ones are involved in $Ca^{2+}$ binding? Second, what is the topology of $Ca^{2+}$ binding? Third, how does $Ca^{2+}$ binding enhance FP-induced membrane ordering? Fourth, do separate FPs function as do the FP trimers on the whole S protein of the viral membrane? For this purpose, we systematically introduced mutations on those residues and examined their effect on membrane structure as well as their $Ca^{2+}$ binding. We also used a more advanced pseudotyped virus particle (PP)-small unilamellar vesicle (SUV) system to investigate the function of FP in the context of the whole protein, which better simulates the "biological scenario" (13), and we compare the results with the those of separate peptides. We also show by the study of several corresponding mutants of the SARS-2 FP that the work on SARS-1 implies similar conclusions for the SARS-2 FP case.

## MATERIALS AND METHODS

### Lipids and peptides

The lipids POPC (1-palmitoyl-2-oleoyl-sn-glycero-3-phosphocholine) and POPS (1-palmitoyl-2-oleoyl-sn-glycero-3-phosphoserine) and the chain spin labels 5PC, 10PC, and 14PC and a head group spin label dipalmitoylphospatidyl-tempo-choline (DPPTC) were purchased from Avanti (Alabaster, AL) or synthesized by our lab according to previous protocols. Cholesterol was purchased from Sigma-Aldrich (St. Louis, MO). All peptides were synthesized by BioMatik (Wilmington, DE) or SynBioSci (Livermore, CA). The sequences of the peptides and the structure of the spin-labeled lipids are shown in Fig. 1 *D*.

### Vesicle preparation

The composition of membranes used in this study is consistent with our previous study (27). The desired amount of POPC, POPS, cholesterol, and 0.5% (mol:mol) spin-labeled lipids in chloroform were mixed well and dried using $N_2$ flow. The mixture was evacuated in a vacuum drier overnight to remove any trace of chloroform. To prepare multilamellar vesicles, the lipids were resuspended and fully hydrated using 1 mL of pH 5 buffer (5 mM HEPES, 10 mM MES, 150 mM NaCl, and 0.1 mM EDTA, pH 5) at room temperature (RT) for 2 h. To prepare SUVs for circular dichroism (CD) and ITC measurements and the PP-SUV system, the lipids were resuspended in pH 5 buffer and sonicated in an ice bath for 20 min or until the suspension became clear. The SUV solution was then further clarified by ultracentrifugation at 13,000 rpm for 10 min.

### CD spectroscopy

The CD experiments were carried out on an Aviv CD spectrometer (model 215). The peptides were mixed with SUVs in 1% peptide/lipid (P/L) ratio

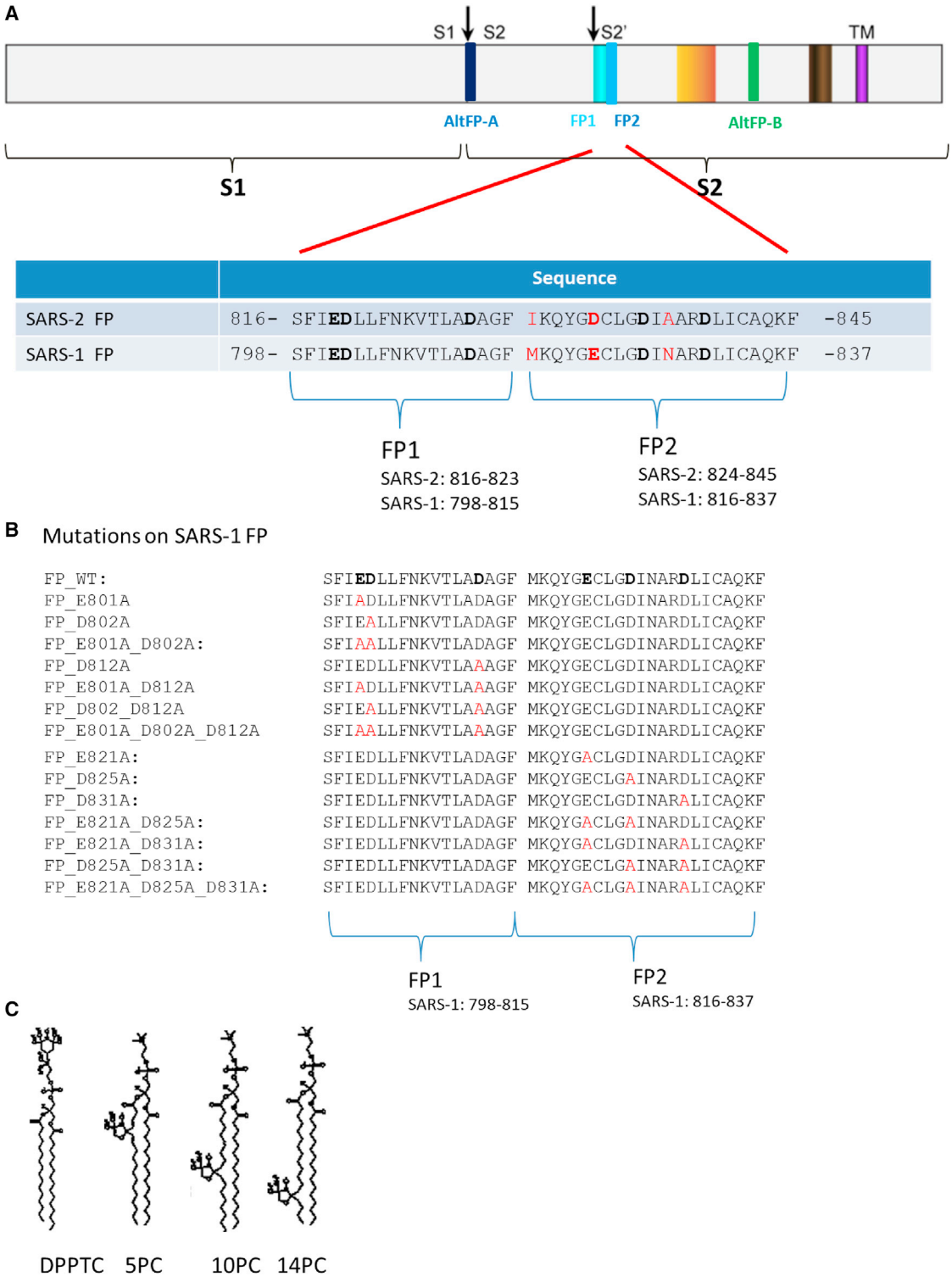


FIGURE 1 (*A*) Diagram of subunits and domains of the S proteins of the SARS-1 and SARS-2 (upper panel) and the sequence alignment of the SARS fusion peptide domain (lower panel). The S protein is cleaved at the S1/S2 site into S1 and S2 subunits. The cleavage at the S2′ site exposes the N-terminal FP domain in the S2 subunit. We designate the FP1 and FP2 segment in the FP (previously designated as FP1_2) as shown in the lower panel. The residues in bold are the negatively charged residues. The residues in red highlight the difference between SARS-2 and SARS-1 FPs. (*B*) The mutations for the SARS-1 FP used in this study. The residues in bold in sequence of the wild-type (WT) are the negatively charged residues. The residue(s) in red indicates where the substitution occurs. (*C*) The structure of spin-labeled lipids used in this study: DPPTC, 5PC, 10PC, and 14PC.

with a final peptide concentration of 0.1 mg/mL at RT for more than 10 min before measurements were made. The measurements were performed at 25°C, and two repetitions were collected. Blanks were subtracted, and the resulting spectra were analyzed. The mean residue weight ellipticity was calculated using the formula $[\Theta] = \theta/(10 \times c \times l \times n)$, where θ is the ellipticity observed (in degrees); $c$ is the peptide concentration (in dmol); $l$ is the path length (0.1 cm); and $n$ is the number of amino acids per peptide (28). The percentages of secondary components were calculated using the online program K2D3 (29).

## ITC

ITC experiments were performed using an N-ITC III calorimeter (TA Instrument, New Castle, DE). To measure the enthalpy of FP membrane binding, FP at 20 μM was injected into 1 mL, 5 mM SUV solution at 37°C. Each addition was 10 μL, each injection time was 15 s, and each interval time was 5 min. Each experiment comprised about 25–30 injections. The data were analyzed using Origin (OriginLab, Northampton, MA).

To measure the peptide-$Ca^{2+}$ interaction, a total of 300 μL, 2 mM $CaCl_2$ in pH 5 buffer was injected into 0.4 mM FP in pH 5 buffer at 37°C in a stepwise manner consisting of 10 μL/injection, except that the first injection was 2 μL. The injection time was 15 s for each injection, and the interval time was 10 min. The background caused by the dilution of $CaCl_2$ was subtracted by using data from a control experiment that titrated $CaCl_2$ in a pH 5 buffer. The data were analyzed using Origin. The one-site model was used in the fitting to calculate the thermodynamic parameters. The protein concentration is determined by dry weight and UV spectroscopy at wavelength = 280 nm with extinction coefficient $\varepsilon = 1520\ M^{-1}\ cm^{-1}$ for SARS-2 and SARS-1 FPs in oxidized condition.

## ESR spectroscopy and nonlinear least squares fit of ESR spectra

To prepare the samples for lipid ESR study, the desired amounts of FPs (1 mg/mL) were added into the lipid multilamellar vesicle dispersion. After 20 min of incubation, the dispersion was spun at 13,000 rpm for 10 min. The concentrations of peptide were measured using UV to ensure complete binding of peptide. The pellet was transferred to a quartz capillary tube for ESR measurement. ESR spectra were collected on an ELEXSYS ESR spectrometer (Bruker Instruments, Billerica, MA) at X-band (9.5 GHz) at 25°C using a $N_2$ temperature controller (Bruker Instruments).

The ESR spectra from the labeled lipids were analyzed using the NLLS fitting program on the basis of the stochastic Liouville equation (30,31) using the microscopic order macroscopic disorder model, as in previous studies (8–11,14). The fitting strategy is described below. We used the NLLS fitting program (30) to obtain convergence to optimum parameters. The g-tensor and A-tensor parameters used in the simulations were determined from rigid limit spectra (8). In the simulation, we required a good fit with a small value of $\chi^2$ and also good agreement between the details of the final simulation and the experimental spectrum. Each experiment (and subsequent fit) was repeated two or three times to check reproducibility and estimate experimental uncertainty. Two sets of parameters that characterize the rotational diffusion of the nitroxide radical moiety in spin labels were generated. The first set is the rotational diffusion constants. $R_\perp$ and $R_\parallel$ are respectively the rates of rotation of the nitroxide moiety around a molecular axis perpendicular and parallel to the preferential orienting axis of the acyl chain. The second set consists of the ordering tensor parameters, $S_0$ and $S_2$, which are defined as follows: $S_0 = \langle D_{2,00} \rangle = \langle 1/2(3\cos 2\theta - 1) \rangle$, and $S_2 = \langle D_{2,0}{}^{2+} D_{2,0\text{-}2} \rangle = \langle \sqrt{(3/2)} \sin 2\theta \cos 2\varphi \rangle$, where $D_{2,00}$, $D_{2,02}$, and $D_{2,0\text{-}2}$ are the Wigner rotation matrix elements, and θ and φ are the polar and azimuthal angles for the orientation of the rotating axes of the nitroxide bonded to the lipid relative to the director of the bilayer (i.e., the preferential orientation of lipid molecules); the angular brackets imply ensemble averaging. $S_0$ and its uncertainty were then calculated in standard fashion from its definition and the dimensionless ordering potentials $C_{20}$ and $C_{22}$ and their uncertainties found in the fitting. The typical uncertainties we find for $S_0$ range from $1 \times 10^{-3}$ to $5 \times 10^{-3}$, while the uncertainties from repeated experiments are $5 \times 10^{-3}$ to $8 \times 10^{-3}$ or less than $\pm 0.01$. $S_0$ indicates how strongly the chain segment to which the nitroxide is attached is aligned along the normal to the lipid bilayer, which is believed to be strongly correlated with hydration/dehydration of the lipid bilayers. As previously described, $S_0$ is the main parameter for such studies (11,32,33).

## PP-SUV docking experiments

The murine leukemia virus-based SARS-1 S-pseudotyped particles, harboring wild-type (WT) SARS-CoV S protein, were generated using a replication-deficient murine leukemia virus core in HEK-293T cell line as previously described (34) and provided by Gary Whittaker and Susan Daniel labs at Cornell. The Western blotting, cell viability assays, and functional pseudotyped virus infectivity assays were also performed in Whittaker and Daniel labs to ensure the expression and the activities of the S-proteins on the PPs. The particle concentration of PPs and the SUVs with spin-labeled lipids were determined using NanoSight NS300 (Malvern Panalytical, Malvern, UK). The PPs were diluted to about $1 \times 10^6$ particle/mL, and the SUVs were mixed in a roughly 1:5 ratio (particle/particle) in the pH 5 buffer at RT transferred in an ESR capillary. The mixture is triggered by the injection of concentrated $CaCl_2$ to make the final $Ca^{2+}$ concentration to 1 mM and immediately start the acquisition. The ESR spectra were collected at RT every 30 s up to the duration of 15 min or longer. The ESR spectra were denoised using the Wavelet Denoising Package (5) as needed, and the local $S_0$ for each spectrum was extracted using the NLSL program (35). The $S_0$-time function were then plotted.

# RESULTS

## Design of peptides and the lipid system

Viral FPs typically have low sequence conservation among different viral groupings. However, they are very well conserved within a given virus family. We previously demonstrated that the SARS-CoV S region immediately downstream of S2′ cleavage site 798–835 (SFIEDLLFNKV TLADAGFMKQYGECLGDINARDLICAQKF) is the bona fide FP. We previously showed that the SARS-1 FP consists of FP1 and FP2 segments; the activity of SARS-1 FP is $Ca^{2+}$ dependent, with its FP1 and FP2 each binding one $Ca^{2+}$ ion (12). (The FP2 segment is sometimes referred as FPPR [20] in the case of the SARS-2 FP). Initially, we also designated region 798–818 as FP1 and region 816–835 as FP2 for the SARS-1 FP (12). However, the boundary between FP1 and FP2 was somewhat arbitrary, as the middle of the FP is a loose linker (36), and in fact there is little overlapping in our earlier designation of FP1 and FP2. Later, from homology comparison and experiments, we identified the corresponding region 816–845 as the FP for SARS-2 (16). In that paper, we designated region 798–817 as FP1 and region 818–835 as FP2 for the SARS-1 FP, with the corresponding region 816–823 as FP1 and 824–845 as FP2 for the SARS-2 FP. We follow this convention in this paper (Fig. 1 *A*). There are six negatively charged residues in the SARS FPs, three in the FP1 region and three in the FP2 region. Those

residues are potentially capable of interacting with the $Ca^{2+}$. However, it is unclear whether they are really involved in $Ca^{2+}$ binding. To examine this, we systematically synthesized mutants with alanine substitution of those residues, and we made single, double, and triple substitutions in both the FP1 and FP2 regions as shown in Fig. 1 *B*.

The ESR signal of spin labels attached to lipids in membrane bilayers is sensitive to their local environment. Four phospholipid spin labels were used: DPPTC has a tempocholine headgroup, and the spin is sensitive to changes of environment at the headgroup region; 5PC, 10PC, and 14PC have a doxyl group in the C5, C10, and C14 position, respectively, of the acyl chain (Fig. 1 *C*); and they are sensitive to the changes of local environment in the hydrophobic acyl chain region at the different depths. Using the NLSL software on the basis of the microscopic order macroscopic disorder model (30,35), the order parameter of the spin can be extracted, which is a direct measure of the local ordering of the membrane. Thus, the effect of peptide binding on the structure of the membrane can be monitored. These four spin-labeled lipids have been used in previous studies, and their ability to detect changes in membrane structure has been validated (37,38). Our previous studies examined the effect of various viral FPs, including those of influenza (8,11), HIV (10), dengue virus (14), ebolavirus (EBOV) (13), SARS-1 (12), MERS (15), and SARS-2 (16), as well as the FP of the ancestral eukaryotic gamete fusion protein HAP2 (14). All of these peptides were found to induce membrane ordering in the headgroup region as well as in the shallow hydrophobic region of bilayers (i.e., 5PC); and this membrane ordering activity for the corresponding nonfusion mutants is either significantly reduced or totally eliminated. Thus, we proposed and repeatedly proved that membrane ordering is the first step of membrane fusion, and "membrane ordering activity" of FPs is a prerequisite for their "membrane fusion activity." To avoid confusion, we use "membrane ordering activity" or "ordering activity" for short whenever we discuss the ESR results.

We used POPC/POPS/Chol = 3:1:1 (molar ratio) as the model membrane system in order to be consistent with the previous studies (12). PS is an anionic lipid that is found in the inner leaflet of the cytosolic membrane and to some extent in endosomal membranes (39). It is critical for synaptic membrane fusion (40–42), and it also promotes viral entry of various viruses (43,44). The PS was shown to be critical for HIV entry as well (45). This composition has been widely used in FP research (46,47). It is also consistent with the system that we have used previously (27). However, we previously used multilamellar vesicles (10,11,14). We used SUV in this ESR study, which is better for comparison with our PP study, also described in this work. And we found that the FP-induced membrane ordering effects for the individual FP and PP systems are similar but not identical.

## The D812A mutant in the FP1 segment provides the largest reduction in its membrane ordering effect

We first considered mutants in the FP1 segment. As shown in Fig. 2 *A*, when the peptide/lipid (P/L) ratio of FP WT increases from 0 to 2 mol%, the order parameter $S_0$ of DPPTC increases significantly from 0.44 to 0.48 at pH 5. This increase of $S_0$ is similar to the effect of influenza FP, as we have previously shown (11). All three single mutants E801A, D802A, and D812A have reduced membrane ordering compared with the WT (cf. Fig. 2 *A*). While the E801A only has a small reduced ordering, that of D802A decreases somewhat more significantly. However, the ordering effect of D812A decreases the most. In fact, its reduction is very similar to that of the E801A_D802A double mutant and only slightly greater than that of the E801A_D802A_D812A triple mutant. It is worth pointing out that the triple mutant still has a residual ordering effect, which is due to two factors. First, SARS-1 and SARS-2 have a "basal" ordering activity even in the absence of $Ca^{2+}$, as we have shown previously (16). Second, even though when all negatively charged residues in the FP1 segment are substituted, the FP2 segment remains unchanged; and we have shown previously that the FP2 by itself also mediates membrane ordering, though to a smaller extent than does FP1 (12).

The membrane ordering of 5PC induced by the FP WT and its mutants also has a similar pattern (Fig. 2 *B*). $S_0$ significantly increases from 0.51 to 0.62 at pH 5 when the FP WT concentration increases. While all mutants yield a reduced ordering, the D812A mutant exhibits the greatest reduction of those three single mutants. In fact, its maximal $S_0$ at 2% P/L ratio is slightly lower than that of the E801A_D802A double mutants. The triple mutant has the lowest ordering activity. Again, even the triple mutant has some "basal" ordering activity, as explained above. The reduction for 5PC is significantly greater than that for DPPTC. This is consistent with the fact that the ordering effect of the WT itself on 5PC is stronger than that on DPPTC. We suggest that the major portion of the FP docks in the shallower hydrophobic region, and thus the membrane order in this region is the most sensitive to the FP. As a result, the effect of the mutation is also most significant in the 5PC region.

From the data of Fig. 2 *A* and *B*, we plot the maximal $\Delta S_0$, which is calculated as $\Delta S_0 = S_0$ (at 2% P/L ratio) $- S_0$ (at 0% P/L ratio) for both DPPTC and 5PC cases (Fig. 2 *C* and *D*, respectively). We also include the results of the other two double mutants E801A_D812A and D802A_D812A, which are not shown in Fig. 2 *A* and *B*. Those two double mutants have a membrane ordering activity similar to the D812A mutant in the headgroup region (DPPTC; Fig. 3 *C*), but their perturbation of the shallow hydrophobic region (5PC) is significantly smaller than that of D812A, especially for the D802A_D812A (Fig. 2 *D*).

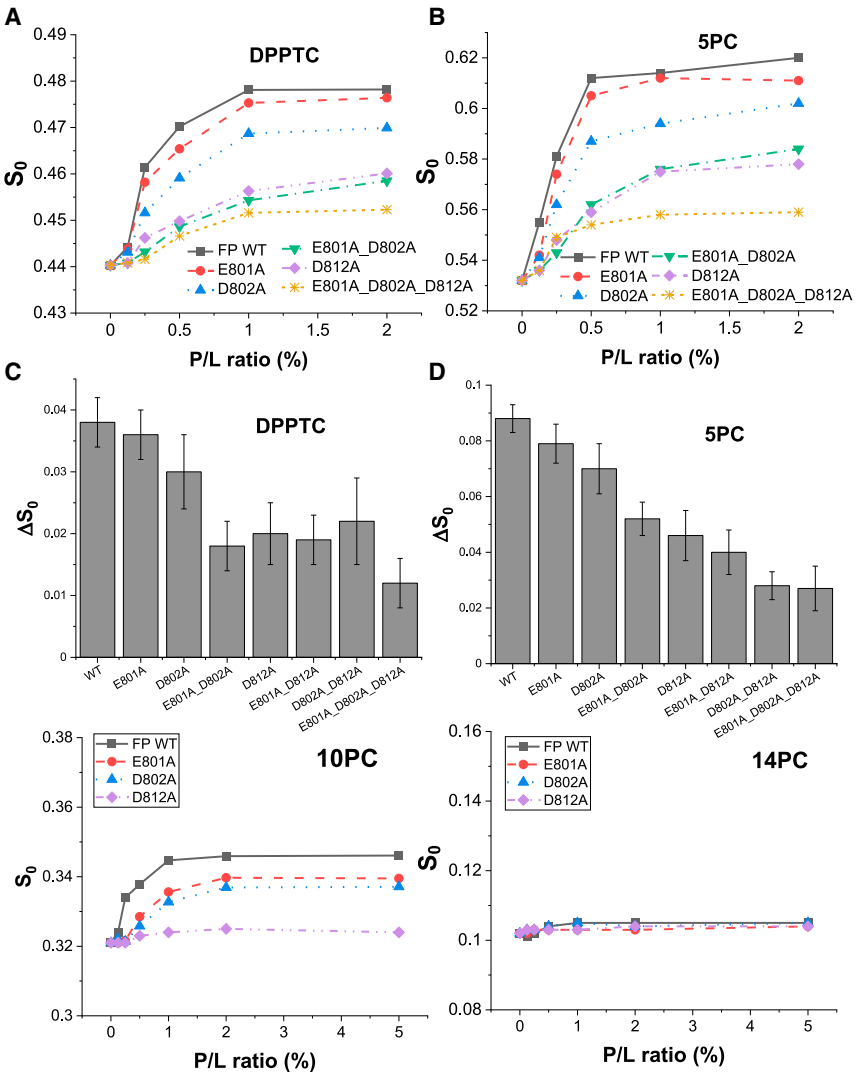


FIGURE 2 Membrane ordering for SARS-FP mutants in FP1 segment. (*A*, *B*, *E*, and *F*) Plots of order parameters of DPPTC (*A*), 5PC (*B*), 10PC (*E*), and 14PC (*F*) versus peptide/lipid (P/L) ratio of SARS-1 FP in POPC/POPS/Chol = 3:1:1 SUV in pH 5 buffer with 150 mM NaCl at 25°C. Black/squares, WT; red/circles, E801A; blue/upward triangles, D802A; green/downward triangles, E801A_D802A; purple/diamonds, D812A; yellow/stars, triple mutants. (*C* and *D*) The plot of $\Delta S_0$ for the WT and mutants of DPPTC (*C*) and 5PC (*D*) at P/L ratio = 2%. $\Delta S_0$ is calculated as $S_0$(2% P/L) − $S_0$(0% P/L). The experiments are typically repeated three times. The typical uncertainties we find for $S_0$ range from $1 \times 10^{-3}$ to $5 \times 10^{-3}$, while the uncertainties from repeated experiments are 5 x $10^{-3}$ to $8 \times 10^{-3}$, or less than $\pm 0.01$.

We also performed this experiment for spin labels 10PC and 14PC, which correspond to the middle hydrophobic region and deep hydrophobic region, respectively. The FP WT can induce membrane ordering at the 10PC region, while neither FP1 and FP2 can (12). Thus, the membrane ordering effect in the middle hydrophobic region can be regarded as a cooperative effect between these two segments. As shown in Fig. 2 *E*, even though E801A has only slightly less ordering activity than that of the WT in the DPPTC and 5PC regions, its ordering activity reduces more significantly in the 10PC region. The D812A has essentially no ordering effect on 10PC at all. The interaction of FPs with lipid bilayers has virtually no effect on the $S_0$ of 14PC even for the WT (Fig. 2 *F*).

Thus, although all single mutants show a reduced ordering activity, the extents of the reduction are different. The mutated versions of the first two negatively charged residues, E801 and D802, have the smallest effect (Fig. 2 *A–D*). Considering that they are next to each other's locations, it is reasonable to suggest that their $Ca^{2+}$ binding functions are redundant. When one has something else substituted for it, the other can assume most of its $Ca^{2+}$ binding function. On the other hand, D812 is the most important residue. Its mutation causes the most substantial reduction of ordering activity of all single mutants. Its ordering activity in the DPPTC and 5PC region is significantly lower than those of E801A and D802A and in fact is very close to the double mutant E801_D802 (Fig. 2 *A–D*). The ordering activity of D812A is very low in the region of 10PC (Fig. 2 *E*).

## All three negatively charged residues in the FP2 segment contribute to the membrane ordering effect comparably

We then studied the mutants in the FP2 segment. As shown in Fig. 3 *A*, all the three single mutants E821A, D825A, and D881A have a significantly lower membrane ordering activity than that of the WT. While the membrane ordering

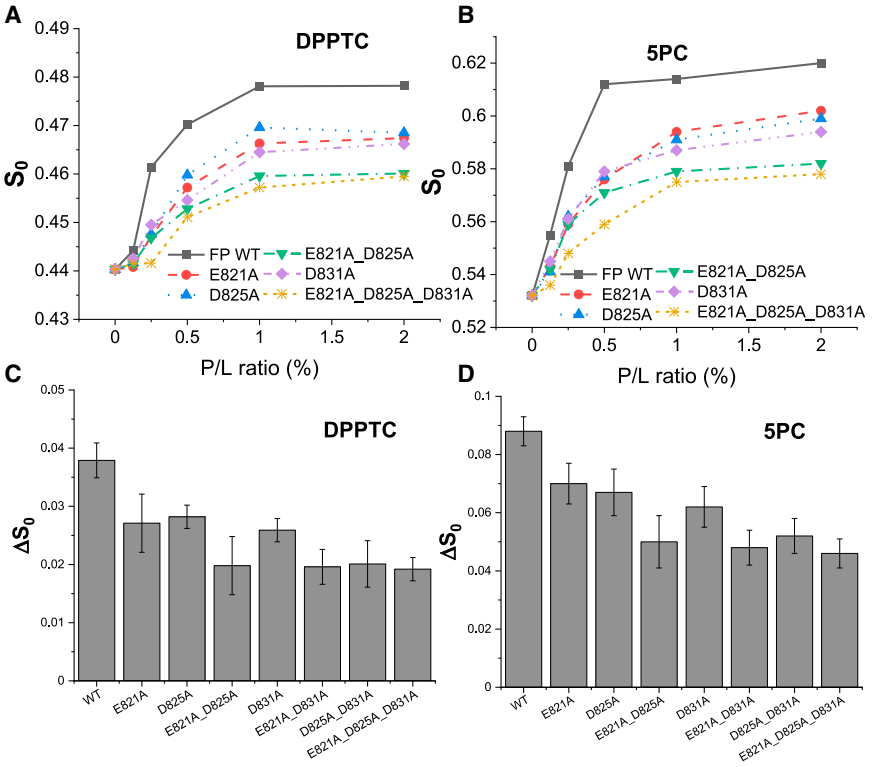


FIGURE 3 Membrane ordering for SARS-FP mutants in FP2 segment. (*A* and *B*) Plots of order parameters of DPPTC (*A*) and 5PC (*B*) versus peptide/lipid (P/L) ratio of SARS-1 FP in POPC/POPS/Chol = 3:1:1 SUV in pH 5 buffer with 150 mM NaCl at 25°C. Black/squares, WT; red/circles, E821A; blue/upward triangles, D825A; green/downward triangles, E821A_D825A; purple/diamonds, D831A; yellow/stars, triple mutants. (*C* and *D*) The plot of $\Delta S_0$ for the WT and mutants of DPPTC (*C*) and 5PC (*D*) at P/L ratio = 2%. $\Delta S_0$ is calculated as $S_0$(2% P/L) − $S_0$(0% P/L). The experiments are typically repeated three times. The typical uncertainties we find for $S_0$ range from $1 \times 10^{-3}$ to $5 \times 10^{-3}$, while the uncertainties from repeated experiments are $5 \times 10^{-3}$ to $8 \times 10^{-3}$, or less than $\pm 0.01$.

among them may show slight differences, they are very similar, which is greater than that of E801A and D802A, but smaller than that of D812A. This is clearly shown in the maximal $\Delta S_0$ plot (Fig. 3 *C*; again $\Delta S_0$ is calculated as $\Delta S_0 = S_0$ [at 2% P/L ratio] − $S_0$ [at 0% P/L ratio]). Interestingly, all three double mutants have low ordering, nearly as low as the triple mutant. This pattern is different from the mutants in the FP1 segments, in which the triple mutant has a significantly lower ordering activity than the double mutants. This pattern is also reflected in the results for 5PC (Fig. 3 *B* and *D*). The three single mutants have a similar level of membrane ordering activity, which is lower than that of the WT. The double mutants and the triple mutants have a similar and even lower level of ordering activity. This strongly suggests that E821, D825, and D831 bind to an ion together and share the contribution almost equally. On the other hand, the $\Delta S_0$ for the mutants in the FP1 regions (Fig. 2 *C* and *D*) do not have such a clear-cut effect at 2% P/L ratio, suggesting the contributions of those three residues are uneven. All mutants basically have no ordering activity in the middle and deep hydrophobic regions (not shown).

Thus, to summarize, all three negatively charged residues in the FP2 segments contribute to the membrane ordering essential equally. This is different from the negatively charged residues in the FP1 segments. The D812 residue is obviously more important than either of the E801 or D802. In fact, its contribution to membrane ordering activity is almost equal to that of E801 and D802 combined, in the E801A_D802A double mutant.

## Increased $Ca^{2+}$ concentration promotes the formation of secondary structures and membrane ordering

To investigate why the membrane ordering effect of SARS-1 FP is $Ca^{2+}$ dependent, we used CD spectroscopy to examine the secondary structure of the FP in membranes with different $Ca^{2+}$ concentrations, which allows us to monitor the structural transitions occurring. As shown in Fig. 4 *A*, the FP has a greater ellipticity at 1 mM $Ca^{2+}$ condition than for 1 mM EGTA at pH5 with SUV in a 1:100 P/L ratio, indicating that it contains more helical component. Using the H2D3 software (29), we can estimate the percentage of alpha helix and beta strand components in the CD spectra. In the presence of 1 mM $Ca^{2+}$, it has 15.6% helix and 14.8% beta strand, and in the absence of $Ca^{2+}$, it has 9.4% helix and 17.2% beta strand. We collected CD spectra in various $Ca^{2+}$ concentration and calculated the helical percentage and then plotted the helical percentage versus $Ca^{2+}$ concentration (inlet of Fig. 4 *A*). We found that the helical concentration increases from 9% at 0 mM $Ca^{2+}$ to 18% at 2% $Ca^{2+}$, which is mostly saturated, and the $X_{50}$ point (the concentration of $Ca^{2+}$ to allow half of the maximal membrane ordering), is about 0.8 mM. Although the change is not dramatic, it is significant and indeed shows a clear trend. Thus, $Ca^{2+}$ promotes the

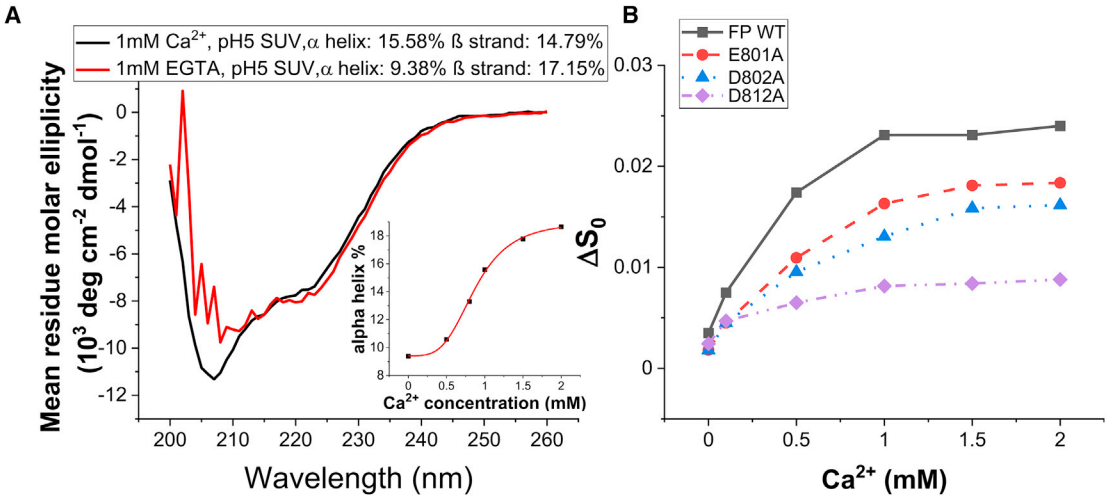


C

| | WT | E801A | D802A | D812A | E821A | D825A | D831A |
|---|---|---|---|---|---|---|---|
| Max($\Delta S_0$) | 0.021 | 0.020 | 0.019 | 0.015 | 0.018 | 0.019 | 0.018 |
| $X_{50}$(mM) | 0.32 | 0.54 | 0.94 | 0.84 | 0.72 | 0.69 | 0.65 |
| Hill Slope (p) | 1.56 | 1.26 | 0.92 | 0.69 | 0.97 | 0.86 | 1.02 |

FIGURE 4 The effect of $Ca^{2+}$ concentration. (*A*) CD spectra of WT FP in membrane at 25°C at pH 5 with 1 mM $Ca^{2+}$ (black/smoother) and 1 mM EGTA (red/jagged). The inlet shows the alpha helix content percentage versus $Ca^{2+}$ concentration. (*B*) The plot of different of order parameters of DPPTC between with and without peptide binding ($\Delta S_0$) versus $Ca^{2+}$ concentration in POPC/POPS/Chol = 3:1:1 SUV in pH 5 buffer with 150 mM NaCl at 25°C. Black/squares, WT; red/circles, E801A; blue/upward triangles, 802A; purple/diamonds, D812A. (*C*) The parameters Max($\Delta S_0$), $X_{50}$, and Hill slope were obtained from the fittings of (*B*) using the logistic function $\Delta S_0 = \frac{\Delta S_{0,min} - \Delta S_{0,max}}{1+(X/X_{50})^p} + \Delta S_{0,max}$.

folding of the FP in the membrane. This is consistent with the results we obtained from SARS-2 FP (16).

## The mutations reduce the response to $Ca^{2+}$ in the ordering

To investigate the effect of the $Ca^{2+}$ concentration, we repeated the ESR experiment using DPPTC. This time, however, we fixed the P/L ratio, increased the $Ca^{2+}$ concentration from 0 to 2 mM, and extracted the $S_0$. The greatest calcium concentration used here is greater than extracellular concentrations of $Ca^{2+}$ in human adult lungs (about 1.3 mM) (48), and from the CD experiments we know that 2 mM $Ca^{2+}$ has already saturated the structural change of the FP. The increase in $S_0$ has two sources, the FPs and the $Ca^{2+}$; thus, we generated a $\Delta S_0$-$Ca^{2+}$ concentration plot, where $\Delta S_0 = S_0$ (membrane with 1% FP) $- S_0$ (membrane without FP) at each $Ca^{2+}$ concentration. This subtraction cancels the membrane ordering induced by $Ca^{2+}$ only (although it is relatively small), with $\Delta S_0$ at each $Ca^{2+}$ concentration representing only the contributions of the FPs. As shown in Fig. 4 *B*, $Ca^{2+}$ increases the $\Delta S_0$ of the FP WT; thus we call it the "$Ca^{2+}$ response effect." This $Ca^{2+}$ response effect gets saturated when the $Ca^{2+}$ concentration exceeds 1 mM. This $Ca^{2+}$ response effect reflects how the binding of $Ca^{2+}$ of the FP promotes the folding of the FP in membrane and thus enables the FP to induce a greater ordering effect. We performed the same experiments on the six single mutants in both the FP1 and FP2 segments. If a mutant has a flatter $Ca^{2+}$ response, then the corresponding mutated residue has a greater contribution in the $Ca^{2+}$ binding. As shown in Fig. 4 *B* for the three mutants in the FP1 segment, D812A again shows a flat $Ca^{2+}$ response compared with the WT; and the $Ca^{2+}$ responses of E801A and D802A are flatter than that of the WT but still significantly steeper than that of the D812A. We fitted the curves with the logistic function $\Delta S_0 = \frac{\Delta S_{0,min} - \Delta S_{0,max}}{1+(X/X_{50})^p} + \Delta S_{0,max}$ with fixed $S_{0,min}$ and flexible $S_{0,max}$ and also extracted the parameters of Max($\Delta S_0$), $X_{50}$, and Hill slope (p) from the curves (Fig. 4 *C*). Max($\Delta S_0$) indicates the maximal boost of the $Ca^{2+}$ to the membrane ordering effect induced by the FPs. As shown in Fig. 4 *C*, the Max($\Delta S_0$) of D812A is only 0.015, which is much smaller than the WT (0.021). The Max($\Delta S_0$) for the three single mutants in the FP2 segments

are again very similar, which is consistent with the results showing that they contribute equally to the $Ca^{2+}$ binding.

### The A811D substitution rescues the reduced ordering activity of D812A

From the results above, we find that the D812 is a key residue. We want to see whether this is related solely to its charge. Thus, we mutated a residue next to D812, A811 to D in both the WT (so we have A811D) and the D812A (so we have A811D_D812A), and repeated the ESR experiments (Fig. 5 *A*). The hypothesis is that if the charge is the only reason for its importance in $Ca^{2+}$-dependent membrane ordering, then for the A811D_D812A, the substitution of Asp for Ala at position 811 could "rescue," at least partially, the "loss of $Ca^{2+}$ binding function" of the substitution of Ala for Asp at position 812. And for the A811D, the two changed residues side by side will increase the binding of $Ca^{2+}$. As shown in Fig. 5 *B* and *C*, the $\Delta S_0$ of DPPTC significantly increases to 0.034 induced by 2% P/L ratio of the double mutant A811D_D812A, which is close to that induced by the same amount of WT (0.038). The A811D mutant actually induces an even greater ordering ($\Delta S_0$ = 0.040) than the WT, but the difference is not statistically significant. For the $\Delta S_0$ of 5PC, the double mutant rescues even more ordering activity than it does in the DPPTC case, as the $\Delta S_0$ is almost equal to that of the WT. The A811D mutant shows a little greater ordering activity than the WT in the case of 5PC, though the difference is not statistically significant either. We also repeated the ESR experiment for the $Ca^{2+}$ response. As shown in Fig. 5 *D*, both the double mutant and A811D have a $Ca^{2+}$ response similar to that of the WT, and both much greater than that of the D812A. Thus, the data suggest that the "loss of function" of the D812 → A substitution can be largely rescued by the A811 → D substitution. The reason why the A811 → D substitution cannot fully rescue the ordering activity may be due to the unfavorable spatial position when D811 binds the $Ca^{2+}$ ion compared with when the native D812 does. The fact that the A → D substitution (A811D) does not

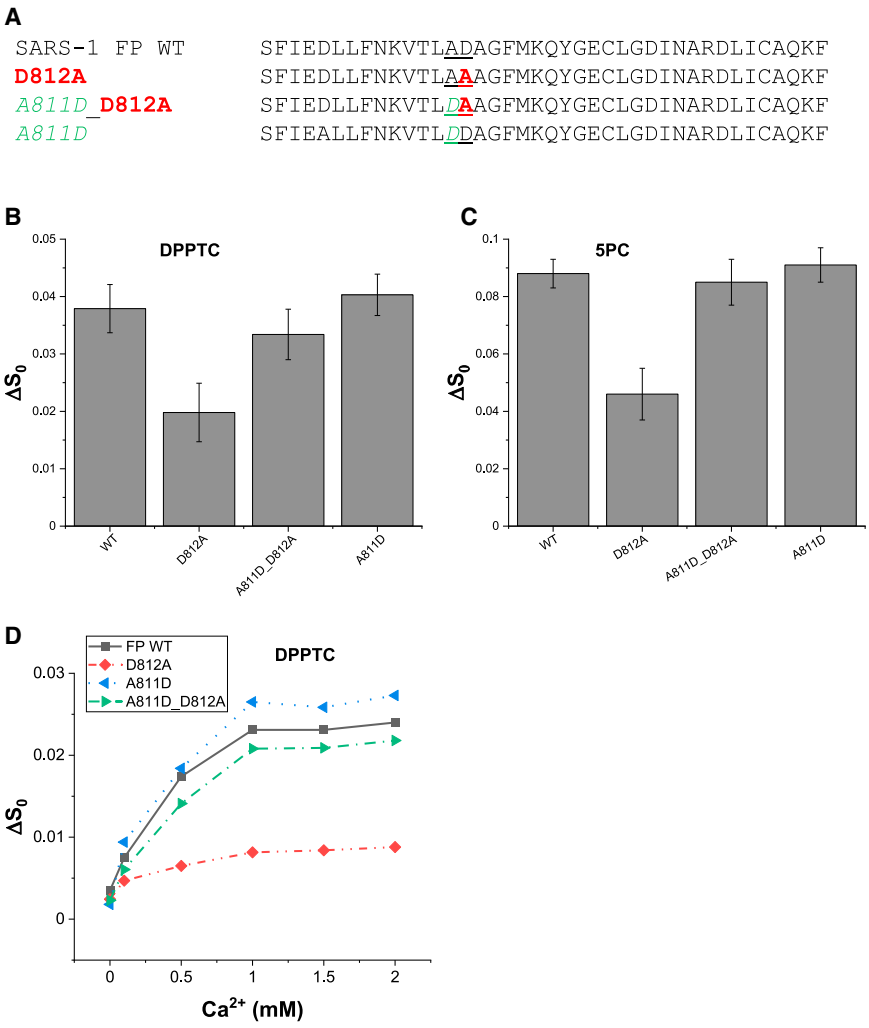


FIGURE 5 The substitution of A811D rescues the reduced ordering activity of D812A. (*A*) The sequence of WT FP, D812A, A811D, and A811D_D812A, with the WT FP underlined. The residue in red/bold highlights the D812A, and the residue in green/italic highlights A811D. (*B* and *C*) The plot of $\Delta S_0$ of DPPTC (*B*) and 5PC (*C*) for the WT and mutants of DPPTC. (*D*) The plot of different parameters of DPPTC between with and without peptide binding ($\Delta S_0$) versus $Ca^{2+}$ concentration in POPC/POPS/Chol = 3:1:1 SUV in pH 5 buffer with 150 mM NaCl at 25°C. Black/squares, WT; red/diamonds, D812A; blue/left triangles, A811D; green/right triangles, A811D_D812A. The experiments are typically repeated three times.

significantly increase the ordering activity of the FP indicates that one charged residue is strong enough to bind to the $Ca^{2+}$ from one location, and the additional charged residue in the same location only has a marginal benefit.

## Interactions of FPs with calcium cations detected by ITC

We used ITC to investigate whether $Ca^{2+}$ cations directly interact with SARS-CoV FPs. During titration, $CaCl_2$ was injected into a reaction cell containing FPs. The background caused by the dilution of $CaCl_2$ has been subtracted by using data from a control experiment that titrated $CaCl_2$ in a pH 5 buffer. Substantial heat absorbed during the titration was observed, with the heat absorbed saturating toward the end of the titration. The data were fit using a one-site model, which hypothesizes that all binding sites have the same binding coefficient. While two binding sites may not have the same binding coefficient, especially for some mutants, this model can be used to estimate the "average" binding coefficient ($K_b$) and N ($Ca^{2+}$/FP ratio).

As shown in Fig. 6 *A*, when the heat versus molar ratio plot was fit using a one-site model that assumes that all binding sites have the same binding affinity, we calculated the enthalpy change $\Delta H = 6.77$ kCal/mol, with binding constant $K_b = 2.49 \times 10^4\,M^{-1}$ and stoichiometry $N = 1.70$. From these parameters, we further calculated the free energy change $\Delta G = -RT\ln K_b = 6.49$ kCal/mol and $-T\Delta S = \Delta G - \Delta H = -1.80$ kCal/mol. The data show that the calcium-FP interaction is endothermic, and the binding ratio is close to two calcium ions per peptide. The reason for the endothermic reaction could be because the buffer solution (150 mM NaCl) contains significant amounts of $Na^+$ ions that could also interact with FP and that a stronger binding of $Ca^{2+}$ cations

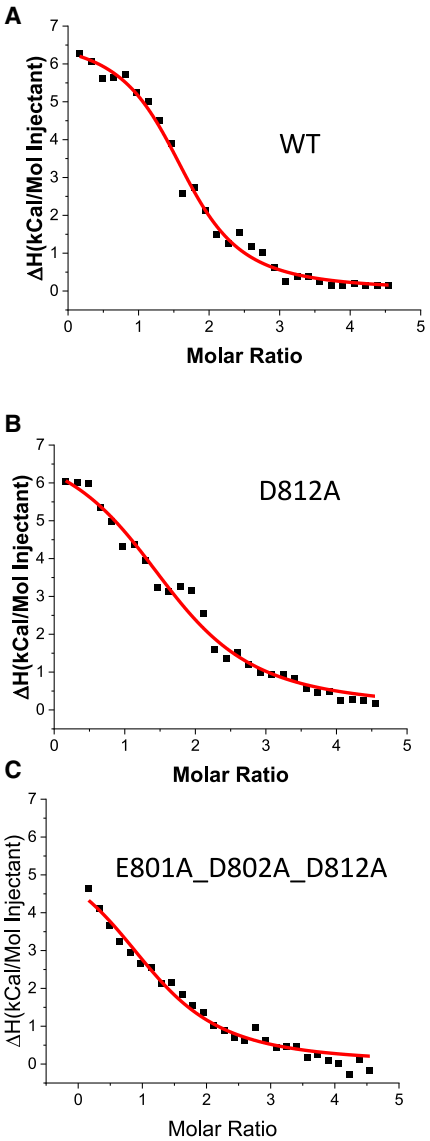


D

| Peptides | ΔH | $K_b$ ($10^4$ $M^{-1}$) | N |
|---|---|---|---|
| SARS-1 WT | 6.77 | 2.49 | 1.7 |
| E801A | 6.86 | 2.56 | 1.73 |
| D802A | 7.21 | 2.35 | 1.69 |
| E801A_D802A | 6.58 | 1.13 | 1.6 |
| D812A | 7.05 | 1.02 | 1.75 |
| E801A_D802A_D812A | 5.97 | 0.80 | 1.19 |
| E821A | 6.54 | 2.15 | 1.65 |
| D825A | 6.67 | 2.06 | 1.63 |
| E821A_D825A | 6.35 | 1.57 | 1.52 |
| D831A | 6.49 | 1.92 | 1.67 |
| E821A_D831A | 6.23 | 1.69 | 1.57 |
| D825A_D831A | 6.55 | 1.72 | 1.58 |
| E821A_D825A_D831A | 6.14 | 1.23 | 1.20 |
| MERS | 3.12 | 1.14 | 1.12 |

FIGURE 6 ITC analysis of $Ca^{2+}$ binding to FP of the coronaviruses. (*A*) SARS-1 FP, (*B*) D812A, and (*C*) triple mutant (E801A_D802A_D812A). The peptides were titrated with $CaCl_2$ in the pH 5 buffer. The integrated data represent the enthalpy change per mole of injectant, ΔH, in units of kcal/mol as a function of the molar ratio. The experiments were duplicated. The data were fitted using a one-site model. Data points and fitted data are overlaid. (*D*) parameters of the FP-$Ca^{2+}$ titration obtained from the ITC curves using one-site model.

displaces bound $Na^+$ into the bulk solution. The ITC experiments we conducted demonstrate strong evidence for direct calcium-FP interactions. We performed this experiment for the mutants as well. As shown in Fig. 6 *B*, the D812A mutant has a very similar ΔH as the WT, and the binding stoichiometry N = 1.75 is not so different from that of the WT as well. However, its slope is flatter, which reflects a weaker binding constant. The triple mutant E801A_D802A_D812A also has an even flatter slope (Fig. 6 *C*), and its enthalpy is significantly smaller (5.97 kCal/mol); and most important, the binding stoichiometry N = 1.19, which is very close to that of MERS FP. MERS FP has known to bind only one $Ca^{2+}$ ion, not two (15). Thus, the triple mutant only binds one $Ca^{2+}$, which is consistent with the fact that all negatively charged residues in FP1 segment are substituted. We repeated the experiments for other mutants and list the parameters in Fig. 6 *D*. The triple mutant in the FP2 segment gives N = 1.20, which is also close to that of the MERS FP (i.e., has only one binding site).

## Enthalpy changes of FP and membranes interaction

As we have shown in the CD experiment, $Ca^{2+}$ promotes the folding of the FP in the membranes. The folding of the FP can be further analyzed by comparing membrane binding enthalpies of FPs measured by ITC. To measure the binding enthalpy, small amounts of peptide were injected into a reaction cell containing a large excess of SUV lipid membranes. Thus, during the whole titration process, the amount of available membrane can be regarded as constant, and all injected peptides can be regarded as binding to the membranes. As a result, the reaction heat in each injection is equal. The enthalpy of reaction can be calculated from the average of heat in each injection (28,49). The FP-membrane participation is driven by enthalpy and opposed by the entropy, as previously shown (50). We performed the experiments under two conditions, in the presence of 1 mM $Ca^{2+}$ and in the presence of 1 mM EGTA. In both cases, the same concentration of $Ca^{2+}$ or EGTA are present in both the reaction cell and the injection syringe. Thus, there is no heat generated because of the $Ca^{2+}$-peptide or the $Ca^{2+}$-membrane interaction. Therefore, the heat detected is generated only from the membrane-FP interaction. The enthalpy gain (more negative enthalpy) is due largely to the formation of hydrogen bonds when the FP adopts a relatively fixed secondary structure when transferred from the solution (in which it is largely unstructured) to the membranes. A more negative enthalpy during the membrane binding reflects a better folding in the membrane.

We first examined the ΔH in the presence of $Ca^{2+}$. As shown in Fig. 7 *A*, the WT folds the best in membranes, as it has the greatest enthalpy gain (most negative), while the triple mutants E801A_D802A_D812A and E821A_D825A_D831A fold worst in membranes. If we compare all single mutants, the D812A again has significantly smaller enthalpy gains than either the E801A and D802A, which is consistent with the previous ESR results showing that this mutant has the lowest membrane ordering activity and lowest $Ca^{2+}$ response. By comparing the ΔHs in the presence and absence of $Ca^{2+}$, we found a pattern that for all WT and mutants, the enthalpy gain ΔH in the presence of $Ca^{2+}$ is greater (more negative) than that in the absence of $Ca^{2+}$. This indicates that the FPs fold better in membranes in the presence of $Ca^{2+}$ in general. We also found that the ΔH and mutations are correlated well in both conditions (i.e., if a mutant has a greater enthalpy gain in the presence of $Ca^{2+}$, it will have a greater enthalpy gain in the absence of $Ca^{2+}$). We further calculated the difference of ΔHs between these two conditions and obtained ΔΔH = ΔH(with Ca) − ΔH(without Ca), as shown in Fig. 7 *B*. This ΔΔH represents how much better folding of the FP in the presence of $Ca^{2+}$. The greater ΔΔH (more negative) indicates the greater effect of $Ca^{2+}$ to promote the folding of the FP in membranes, which is related to the CD (Fig. 4 *A*) and $Ca^{2+}$ response results investigated using ESR (Fig. 4 *B*). We found that the two triple mutants have the smallest ΔΔH (−2.1 and −1.5 kCal/mol, respectively), while the WT has the greatest ΔΔH (−9.9 kCal/mol). This indicates that WT folds in the membrane much better in the presence of $Ca^{2+}$ than in the absence of $Ca^{2+}$, suggesting that the $Ca^{2+}$ promotes the folding of WT most effectively. For all single mutants, D812A has the smallest ΔΔH (−5.1 kCal/mol), suggesting $Ca^{2+}$ does not promote its folding as well as the other single mutants, which further indicates the importance of D812 in the FP-$Ca^{2+}$ interaction.

## The mutants of SARS-2 FP show trends similar to the corresponding SARS-1 FP mutants

We initially started this study well before the COVID-19 outbreak. After the outbreak began, we started to work on SARS-2 FP as well. We found that the SARS-2 FP also induces membrane ordering in a $Ca^{2+}$-dependent fashion, and its effect is even greater than that of the SARS-1 FP (16). While we focus mainly on SARS-1 FP in this paper, we continue with parallel research on SARS-2 FP. The sequence of SARS-2 FP only has a three amino acid difference from that of the SARS-1 FP (Fig. 8 *A*), and only one of them is negatively charged, which is E821 in SARS-1 FP and the corresponding D839 in SARS-2 FP (both of them are negatively charged). We expect that the $Ca^{2+}$ binding pattern of SARS-2 FP is similar to that of SARS-1 FP. As shown in Fig. 8 *B* and *C*, D839A (corresponding to E821A in the SARS-1 FP) has a smaller membrane ordering effect than the SARS-2 FP WT in both DPPTC and 5PC cases. And the D830A (corresponding to D812A in the SARS-1 FP) has an even smaller effect than that of D839A. These results are consistent with our findings in the SARS-1 FP on D812A and D821A. Thus, the knowledge

A

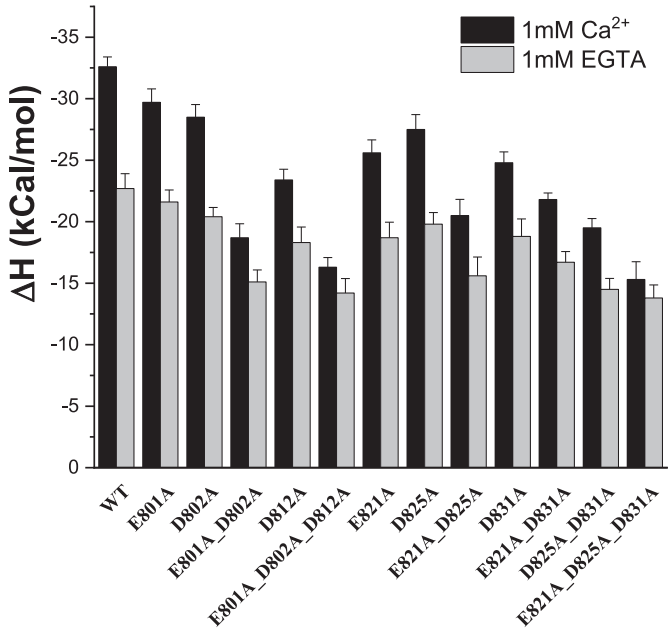


B

| Peptides | ΔΔH=ΔH(w/Ca)-ΔH(w/o Ca) |
|---|---|
| WT | -9.9 |
| E801A | -8.1 |
| D802A | -8.1 |
| E801A_D802A | -3.6 |
| D812A | -5.1 |
| E801A_D802A_D812A | -2.1 |
| E821A | -6.9 |
| D825A | -7.7 |
| E821A_D825A | -4.9 |
| D831A | -6.0 |
| E821A_D831A | -5.1 |
| D825A_D831A | -5.0 |
| E821A_D825A_D831A | -1.5 |

FIGURE 7 ITC analysis of FP-membrane interaction. (*A*) Enthalpy of SARS-1 FP-membrane interaction. The peptides were injected into the reaction cells containing POPC/POPS/Chol = 3:1:1 SUV in pH 5 buffer with 150 mM NaCl at 25 °C in the presence of either 1 mM $Ca^{2+}$ (black) or 1 mM EGTA (gray). The reaction heats of each injection were averaged, and the reaction enthalpy was calculated. The experiments were duplicated. (*B*) The ΔΔH of the WT and mutants, in which ΔΔH = ΔH(with $Ca^{2+}$) − ΔH(with EGTA). This value indicates the difference of membrane binding enthalpy due to the presence of $Ca^{2+}$.

we obtain from this research on SARS-1 FP is also mostly applicable to SARS-2 FP.

## $Ca^{2+}$ promotes insertion of viral S protein trimer into the target membrane in the PP-SUV docking system

It has been questioned whether the FPs by themselves function the same as the FPs in the viral glycoprotein. To address this issue and to better simulate the "biological scenario," we have developed a methodology we call the "PP-SUV docking system" (Fig. 9 *A*) (13). The PPs are nontransmittable chimeric viral particles expressing viral glycoproteins such as SARS-1 S trimers on the surface of a replication-deficient murine virus. The PP with the S protein is pretreated by proteinase. When the PP is mixed with the SUV containing DPPTC, the SARS-1 FP will insert into the SUV membrane during the docking of the PP on the SUV. After mixing the PP and the SUV containing spin-labeled lipids and triggering with $Ca^{2+}$, we collected ESR spectra every 30 s. In order to do that, we needed to reduce the scanning times, which, however, yield noisier signals. These noisier signals were then denoised using the recently developed Wavelet Denoising Package (5) before NLSL analysis, as required. We extracted the local $S_0$ from each spectrum and plotted $S_0$ versus time (13) (Fig. 6 *B–D*). Using this methodology, we monitored in real time how the local membrane ordering develops in the SUV membranes

A

| | | Sequence |
|---|---|---|
| SARS-2 FP WT | 816- | SFI**ED**LLFNKVTLA**D**AGF *I*KQYG***D***CLG**D**I*A*AR**D**LICAQKF |
| SARS-1 FP WT | 798- | SFI**ED**LLFNKVTLA**D**AGF *M*KQYG***E***CLG**D**I*N*AR**D**LICAQKF |
| SARS-2 FP D830A | 816- | SFI**ED**LLFNKVTLA**A**AGF *I*KQYG***D***CLG**D**I*A*AR**D**LICAQKF |
| SARS-2 FP D839A | 816- | SFI**ED**LLFNKVTLA**D**AGF *I*KQYG***A***CLG**D**I*A*AR**D**LICAQKF |

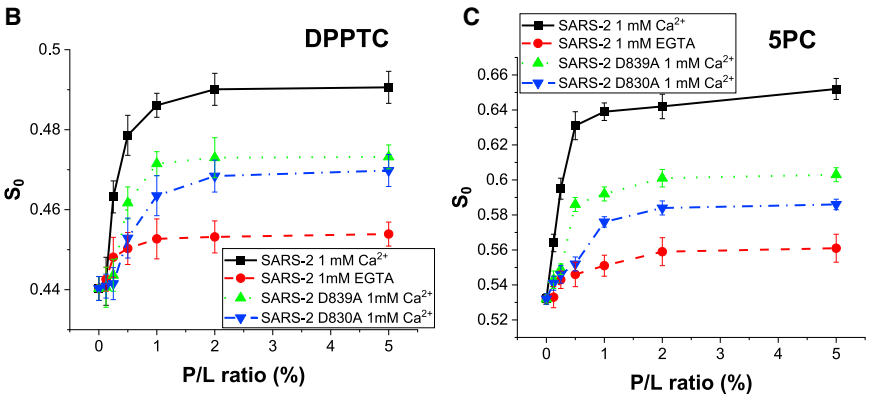


FIGURE 8 Membrane ordering of SARS-2 mutants. (*A*) The sequence of SARS-2 mutants. (*B* and *C*) Plots of order parameters of DPPTC (*B*) and 5PC (*C*) versus peptide/lipid (P/L) ratio of SARS-2 FP in POPC/POPS/Chol = 3:1:1 SUV in pH 5 buffer with 150 mM NaCl at 25°C. Black/squares, WT in the presence of 1 mM $Ca^{2+}$; green/upward triangles, D830A (corresponding to D812A in SARS-1 FP); blue/downward triangles, D839A (corresponding to E821A in SARS-1 FP); red/circles, WT in the presence of 1 mM EGTA. The experiments were repeated three times.

as mediated by the FPs in the whole glycoproteins that are assembled on the PP surface: this better simulates the "biological scenario" (13).

We used EBOV PP as a positive control, as it was shown to work well (13). We fitted the curves using a Boltzmann equation, $\Delta S_0 = \frac{\Delta S_{0,max} - \Delta S_{0,min}}{1+e^{(t-T_{50})/\Delta T}} + \Delta S_{0,min}$, and obtained three parameters from each curve. $\Delta S_{0(max)}$ is the maximal ordering occurs at the end of the time course, indicating the overall ordering activity. $T_{50}$ is the time to reach its 50% maximal ordering effect, indicating how early the PP starts to induce ordering. $\Delta T$ is the slope at $T_{50}$, indicating the rate of the change of $\Delta S_0$, which is how fast the PP induces the ordering once it starts to take effect. The parameters are summarized in Table 1.

As shown in Fig. 9 *B* with DPPTC, for the SARS-1 PP, $\Delta S_0$ increases in the presence of $Ca^{2+}$, and $T_{50}$ occurs at about 3.6 min. If an empty PP (no viral glycoprotein on the surface) was used, there was no increase of $S_0$. Thus, the increase in $S_0$ observed is due to the S protein on the SARS-1 PP. The maximal $\Delta S_0$ of SARS-1 PP is the same as that obtained with just the separate FP (cf. Figs. 2 *A*, *C*, and 9 *E*) and slightly smaller than that of the EBOV PP for which the $T_{50}$ is slightly smaller ($T_{50}$ = 3.2 min). The $\Delta T$ of SARS-1 PP is also slightly greater than EBOV PP (1.19 vs. 1.02 $min^{-1}$). However, this could result from the differences in protein expression level, surface transportation efficiency of the glycoprotein, and/or efficiency of proteinase cleavage. The MERS PP has a significantly slower start ($T_{50}$ = 4.8 min), and once it starts to induce ordering, its $\Delta T$ is also slightly smaller (0.92 $min^{-1}$).

We have previously shown that the $Ca^{2+}$ dependence of SARS-2 FP is very specific (16). We want to test whether this is the case for the SARS-2 and SARS-1 PP. We first compare the triggering effect of $Ca^{2+}$ and $Mg^{2+}$ on SARS-1 PP. As shown in Fig. 9 *C*, the injection of $Mg^{2+}$ instead of $Ca^{2+}$ triggers the $\Delta S_0$ slightly (~0.015 at 15 min), while the $Ca^{2+}$ triggers the $\Delta S_0$ up to ~0.049. There is a signature S-shaped "jump" in the $\Delta S_0$-time curve in the $Ca^{2+}$ case, whereas this shape is not observed in the $Mg^{2+}$ case. If no trigger is added (the same volume of buffer is added instead), the change in $\Delta S_0$ is even smaller, reflecting a "basal" ordering activity. This is consistent with the case for the FP-induced "basal" membrane ordering in the absence of $Ca^{2+}$. These results show that $Ca^{2+}$ is required for the whole S protein on the membrane fusion as expected. We previously noted that there is some "basal ordering activity" for the isolated FP in the presence of EGTA (12,16) (also see Fig. 8 *A*), but the "basal ordering activity" for the whole S protein seems to be negligible as shown in Fig. 9 *C*.

We obtained SARS-2 PP from the Gary Whittaker and Susan Daniel labs and performed a PP study on it, similar to what we did for SARS-1 PP. As shown in Fig. 9 *C* and Table 1, the SARS-2 PP induces an even higher ordering effect than the SARS-1 PP, with a $\Delta S_{0(max)} = 0.058$ compared with SARS-1 PP's 0.049. While it starts the "jump" a little more slowly than the SARS-1 PP, it has a faster rate ($\Delta T$) once it starts to take effect. This is consistent with our previous research that the SARS-2 FP has a higher membrane ordering effect than the SARS-1 FP, even though there are only three residue differences between them (16). We also

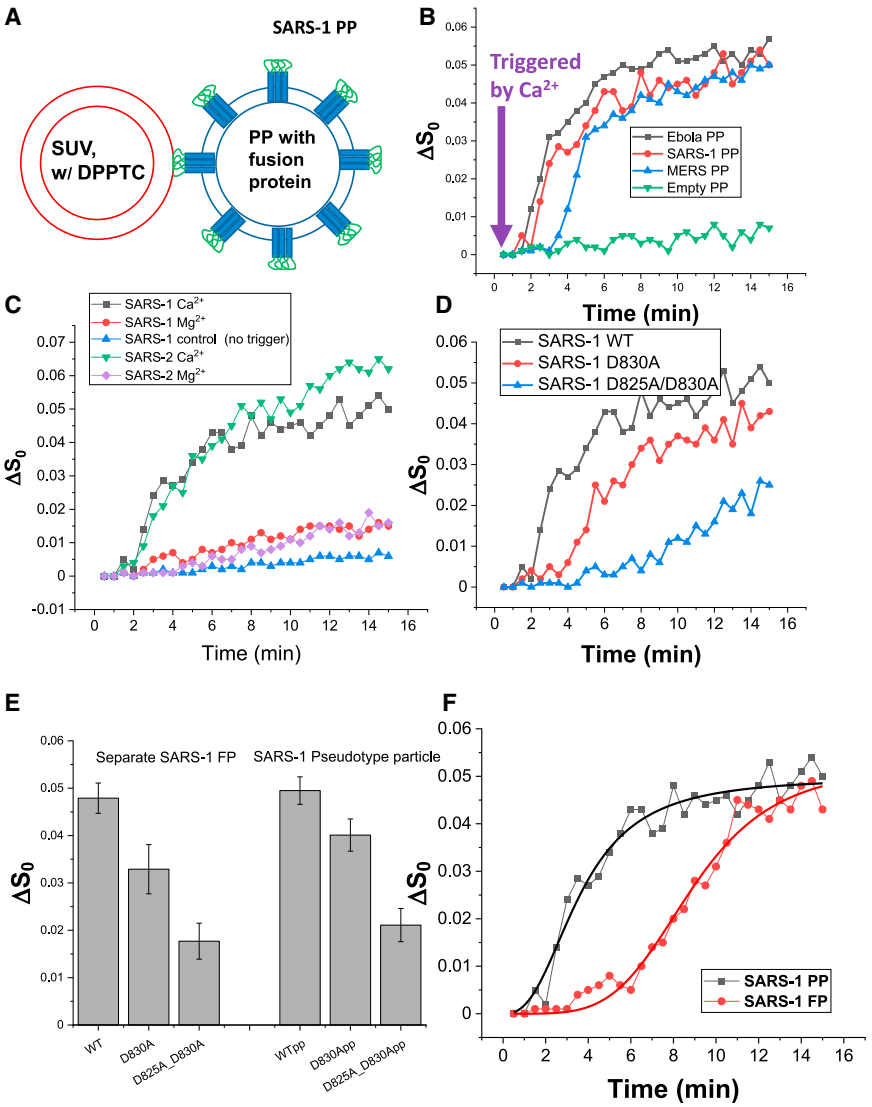


FIGURE 9 Time-dependent ESR experiments in the pseudotype viral particle (PP)-SUV docking system. (*A*) The schematic diagram of the PP-SUV docking system. The fusion protein (in this case EBOV G protein or SARS-1 S protein) were expressed and assembled as trimers on the PP membrane. DPPTC was incorporated in POPC/POPS/Chol = 3:1:1 SUV. The PP and SUV were mixed at a PP:SUV ratio of ∼1:5 and triggered by the addition of 2 mM $Ca^{2+}$. (*B*) The plot of local order parameters of DPPTC changes ($\Delta S_0$) during the time course of measurement. Black, EBOV PP; red, SARS-1 PP; blue, MERS PP; green, empty PP (no viral glycoprotein expressed). (*C*) Same as (*B*) using SARS-1 PP and SARS-2 PP in different triggering conditions. Black, SARS-1 PP triggered by 2 mM $Ca^{2+}$; red, by 2 mM $Mg^{2+}$; blue, control by injecting the same volume of buffer; green, SARS-1 PP triggered by 2 mM $Ca^{2+}$; purple, by 2 mM $Mg^{2+}$. (*D*) Same as (*B*) using wild-type (WT) SARS-1 PP (black), D830A mutant (red), and D825A_D830A double mutant (blue). (*E*) Comparing the $\Delta S_0$ induced by separated FP and PP. (*F*) Comparing the time course of SARS-1 PP (black) and SARS-1 FP (red). In the FP case, we mixed the separate FP and the SUV: the amount of the SUV is the same as the one used in the PP case, and the amount of the FP is 1% of the amount of lipids. The PP has an early start and a steeper slope, while the FP has a late start and a flatter slope although they reach almost the same final $\Delta S_0$.

tested $Mg^{2+}$ as a trigger reagent. As expected, $Mg^{2+}$ cannot trigger the SARS-2 PP to mediate membrane ordering as the $Ca^{2+}$ does. This result confirms that that the $Ca^{2+}$ dependence is very specific for the PP, as shown previously for the SARS-2 FP (16).

We then studied SARS-1 PP mutations. As shown in Fig. 9 *D* and Table 1, the D830A single mutant does exhibit somewhat lower ordering activity than the WT in two ways. First, its $\Delta S_0$(max) (0.040) is less than that of the WT (0.049). Second, its time development ($T_{50}$ = 5.6 min) is slower than that of the WT ($T_{50}$ = 3.6 min). The D825A_D830A double mutant has even lower ordering activity. It has an even smaller $\Delta S_{0(max)}$ (0.035) at the end of our measurement and an even slower time development ($T_{50}$ = 12.3 min). This result suggests that both D830 and D825 are involved in $Ca^{2+}$ binding. The maximal $\Delta S_0$ of the separated WT and mutant FP (from experiments shown in Fig. 3 *A*) and the WT and mutant PP (from Fig. 9 *D*) are compared side by side in Fig. 9 *E*. We can clearly see that the separate FP and the PP induce the ordering in a very similar level. The single mutant of both FP and PP induce a lower ordering, and the double mutant of both FP and PP induce even lower ordering. This result confirms that the knowledge that we obtained from the separate FP mutants can be largely translated to the FP in the context of whole protein in a trimer form anchored on the membrane.

However, we find that the separate FPs function exactly the same way as the PPs, but the kinetics of how the FP and PP induce membrane ordering seem to be different. As shown in Fig. 9 *F*, we compare the FP-induced membrane ordering in a time-dependent experiment with that of the PP. In this experiment, we mixed the FP with SUV in 1% P/L ratio, triggered by the injection of 2 mM $Ca^{2+}$ and collected the ESR spectra just like the procedures we used in the PP-SUV experiment. As we can see, although the $\Delta S_{0(max)}$ for the FP (0.051) is approximately the same

**TABLE 1 The parameters of fittings in PP-mediated membrane ordering**

| | $\Delta S_{0,max}$ | $T_{50}$ (min) | $\Delta T$ (slope) ($min^{-1}$) |
|---|---|---|---|
| Comparison among different PPs | | | |
| EBOV PP | 0.051 | 3.2 | 1.02 |
| SARS-1 PP | 0.049 | 3.6 | 1.19 |
| MERS PP | 0.045 | 4.8 | 0.92 |
| SARS-2 PP | 0.058 | 3.8 | 1.51 |
| Comparison among SARS-1 PP and its mutants | | | |
| SARS-1 PP WT | 0.049 | 3.6 | 1.19 |
| D830A | 0.04 | 5.6 | 1.61 |
| D825A_D830A | 0.035 | 12.3 | 2.98 |
| Comparison between SARS-1 PP and SARS-1 FP | | | |
| SARS-1 PP | 0.049 | 3.6 | 1.19 |
| SARS-1 FP | 0.051 | 8.9 | 4.47 |

The curves are fitted using the Boltzmann function $\Delta S_0 = \frac{\Delta S_{0,max} - \Delta S_{0,min}}{1 + e^{(t-T_{50})/\Delta T}} + \Delta S_{0,min}$.

as that for the PP (0.049), it takes much longer to reach the maximal $S_0$. The $T_{50}$ values are estimated to be 3.6 min for the PP and 8.9 min for the FP (Table 1). And even after the FP starts to perturb the membrane, the rate ($\Delta T$ = 4.47 $min^{-1}$) is much slower than that of the PP ($\Delta T$ = 1.19 $min^{-1}$). Although a careful calibration is required to reach a final conclusion, this likely suggests that the FPs in the whole protein trimer induce membrane ordering more efficiently than the separate FP.

## DISCUSSION

### Which residues contribute to the $Ca^{2+}$ binding?

The mechanism of membrane fusion is still only partially understood. Our past studies have shown that numerous viral FPs induce increased membrane ordering in a collective fashion (i.e., a significant increase in $S_0$ occurs as an "S shape" function of the P/L ratio) (8,9,11–15,51). We have suggested that FP-induced membrane ordering is accompanied with dehydration resulting from peptide insertion, and this is a prerequisite for removal of the repulsive forces between two opposing membranes, thereby facilitating initialization of membrane fusion (8–11,14). In conjunction with our collaborators, we have also determined that the CoVs (SARS-1, SARS-2, and MERS) and EBOV require $Ca^{2+}$ for viral entry and that the $Ca^{2+}$ binding site is on the FP (12,13,16).

Our present study is the first to investigate the $Ca^{2+}$ binding mechanism of CoV FPs in detail at the molecular level using biophysical methods. Although the negatively charged residues can be expected to be related to $Ca^{2+}$ binding, the issues of which residues are involved and how much is its contribution remains unclear. In fact, in the cases of MERS (15) and EBOV (13), not all negatively charged residues are important in the $Ca^{2+}$ binding.

Our results suggest that all negatively charged residues of SARS-1 are involved in $Ca^{2+}$ binding, though they contribute to different extents. While those residues in FP2 (E821, D825, and D831) have almost equal contributions, those of FP1 are more unequal. E801 and D802 seem together to supply a binding site whereas D812 is the most important single residue of all six.

The very low ordering activity of D812A in the middle hydrophobic region (10PC) deserves further discussion. FPs such as that of HA are unable to induce membrane ordering as deep into this region. Neither FP1 and FP2 of SARS-1 can induce membrane ordering in this region as well (12). On the other hand, we have observed a combination of peptides such as the HA FP-TMD dimer can induce membrane ordering in this region, suggesting the ability to induce ordering in this region represents a greater perturbation to the membranes and presumably promotes membrane fusion more efficiently (11). Thus, the ability of the SARS-1 and SARS-2 FPs to induce membrane ordering at the 10PC region may be of significance. Therefore, the lack of any ordering effect for D812A in the 10PC region further indicates the importance of D812. The loss-of-function mutation D812A can be "rescued" by the mutation of a nearby A → D substitution at residue 811, indicating that the $Ca^{2+}$ binding function of D812 is due to its charge.

### What is the $Ca^{2+}$ binding topology?

Even though we have shown that the separate FP1 and FP2 peptides each bind one $Ca^{2+}$ (12), this may not be the case when they are in the context of the full-length FP (also known as FP1_2), as the binding topology could be reshuffled when a total of six negatively charged residues are now present. There could be at least several topological models with different topologies (cf. Fig. 10 *A*). In the first model, FP1 and FP2 each bind one $Ca^{2+}$ (Fig. 10 *A*, left). A second possibility is that the negatively charged residues near the boundary between FP1 and FP2, namely, D812 on FP1 or E821 on FP2 in SARS-1 FP, are involved in the binding of the "ion in the other side," that is, D812 binds an ion in the C-terminal (second $Ca^{2+}$ ion), or E821 binds the ion in the N-terminal (first $Ca^{2+}$ ion) (Fig. 10 *A*, middle, showing the former case). Third, the negatively charged residues in the middle (e.g., D812 and E821) bind one ion, and those in both termini bind the other (Fig. 10 *A*, right).

The reduction of ordering of the mutants investigated by ESR strongly favors the first topological model (Fig. 10 *A*, left); that is, the three residues in the FP1 segment bind one ion, and three residues in the FP2 segment bind another. This model is further supported by the FP-$Ca^{2+}$ binding titration (Fig. 6 *A–D*). We found that only the triple mutants in both FP1 and FP2 segments give an FP1_2:$Ca^{2+}$ binding ratio (N) close to unity. This is consistent with the first model, and contradicts the other models.

If the second model (Fig. 10 *B*) were correct, we would expect the N of E801A_D802A to be close to unity: D812

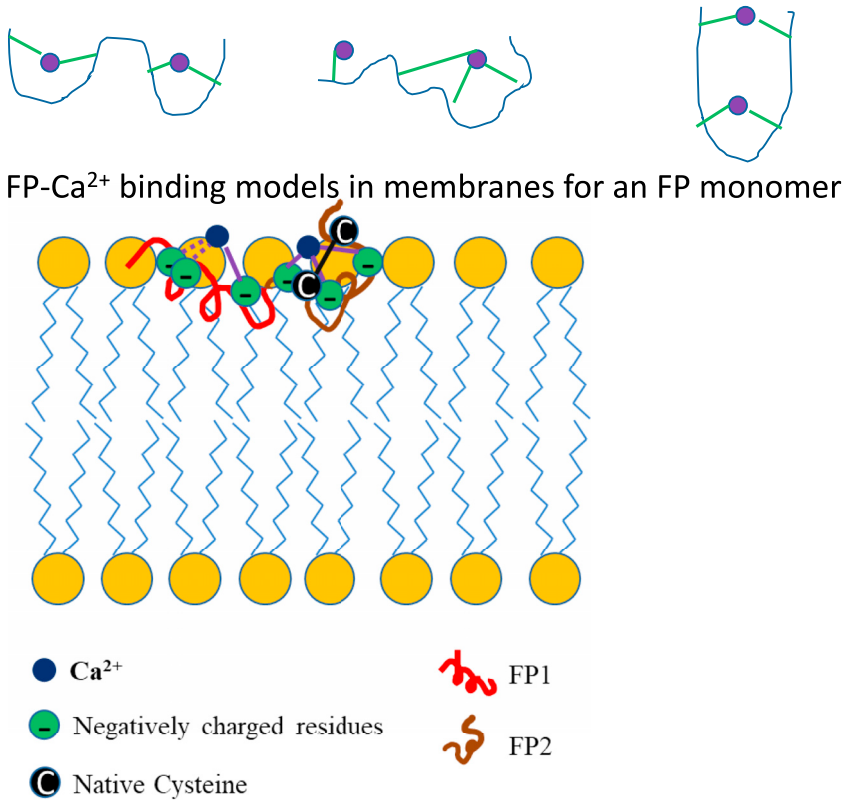


FIGURE 10 (*A*) Different topologies of $Ca^{2+}$ binding models. Left: the three negatively charged residues in FP1 bind one $Ca^{2+}$ ion, and the three negatively charged residues in FP2 bind another. Middle: the negatively charged residues in FP1 in the N terminus binds one $Ca^{2+}$, while the negatively charged residue in FP1 that is close to the FP1-FP2 boundary (i.e., D812) and the three negatively charged residues in FP2 bind another $Ca^{2+}$ ion. Right: the negatively charged residues in both termini bind one $Ca^{2+}$ ion, and the negatively charged residues that are close to the FP1-FP2 boundary bind another Ca2+ ion. (*B*) Model of a single coronavirus FP interacting with a lipid bilayer. This model summarizes the data obtained in this work and highlights the unique features of this FP, including its bipartite nature and calcium-binding ability. FP1 and FP2 each bind one $Ca^{2+}$ ion by all three negatively charged residues located on them. In FP1, E801 and D802 serve together as a binding anchor, and D812 serves as the other anchor. In FP2, E821, D825, and D831 each serve as one anchor. The binding of $Ca^{2+}$ pulls the FP into the hydrophobic and hydrophilic interface via electrostatic interactions between the $Ca^{2+}$ and the negatively charged lipid headgroup and thus promotes the folding of FP in membranes; the $Ca^{2+}$ also "fixes" the conformation of the FP by holding the anchors (as shown in the model in A, left). The disulfide bond between the two cysteines in FP2 also serves as an addition mechanism of "holding" the conformation of FP2. (*C*) Model of the asymmetrically trimerized FPs that insert deeper into the membrane and have a greater effect on membrane ordering. We hypothesize that the trimerization is asymmetric in that FP1 of the first FP unit, the FP2 of the second FP unit, and the FP1 of the third FP unit interact with one another, while the FP2 of the first FP unit, the FP1 of the second FP unit, and the FP2 of the third FP unit interact with one another. The structure of the FP is partially adapted from the NMR structure on the basis of the monomer (23).

binds the second ion but not the first ion, so this double mutant will lose its binding site for the first ion. However, its N is 1.6. The same logic also excludes the possibility that E821 binds the first ion, as the N of D825A_D831A is 1.58.

The third model were also unlikely. If it were correct, the remaining three negatively charged residues in the FP2 segment in triple mutants (in FP1) E801A_D802A_D812A will still bind two ions (for example, E821 binds one ion and D825 and D831 bind the other). But the N of E801A_D802A_D812A is close to 1 (1.19). The same logic is also applied to the result of the triple mutants (in FP2) E821A_D825A_D831A.

Of course, this FP-$Ca^{2+}$ titration is in solution, not in membranes. However, our ITC experiments on FP-membrane interaction support the first model from another perspective. The difference of the partitioning enthalpy $\Delta H$ (Fig. 7 *A* and *B*), with or without $Ca^{2+}$, indicates the folding of FP in the membrane due to the binding of $Ca^{2+}$. Again, we find that the triple mutants have lowest $\Delta\Delta Hs$, indicating only one $Ca^{2+}$ binding. And the three

double mutants in the FP2 segments are very close to each other, indicating a comparable contribution to $Ca^{2+}$ binding that is consistent with our ESR ordering activity results and FP-$Ca^{2+}$ binding results. Comparing the FP-$Ca^{2+}$ titration and the FP-membrane titration results, we found that although the former reaction occurs in solution and the latter in membranes, the FP-$Ca^{2+}$ binding behavior is largely consistent; that is, the mutants with a lower N in the FP-$Ca^{2+}$ titration have a lower $\Delta\Delta H$ value in the FP-membrane titration (Fig. S1). When the FP inserts into membranes, its overall accessibility to $Ca^{2+}$ should be different from that in the solution. However, Fig. SF1 shows that those negatively charged residues are accessible to $Ca^{2+}$ even in membranes.

This model (Fig. 10 *A*) is not fully consistent with a recent NMR study of the structure of SARS-2 FP (23), which suggests that D830 (corresponding to D812 in SARS-1 FP) does not bind to $Ca^{2+}$, and D839 and D843 (corresponding to E821 and D825 in SARS-1 FP) most likely participate in binding $Ca^{2+}$, while the other three are moderately likely to bind $Ca^{2+}$. The NMR study is on SARS-2 FP, so it could be somewhat different from our SARS-1 FP study. But we believe that the environment used in the study, which consists of bicelles composed mainly of DMPC, which lacks negatively charged headgroups such as PS, is a more important factor. The negatively charged headgroups attract $Ca^{2+}$ to the membrane surface and thus increase the $Ca^{2+}$ concentration in the headgroup region. Thus, the failure of attracting $Ca^{2+}$ by the neutral headgroups will significantly reduce the accessibility of the negatively charged residues of the FP to $Ca^{2+}$, thus lowering the interaction between them. In that NMR study, the amide peaks of the backbone only shifted minimally, indicating that the interactions between the FP and $Ca^{2+}$ are indeed minimal in that environment. The cholesterol used in our study also plays a role in the FP-$Ca^{2+}$ interaction given that cholesterol decreases the fluidity of the membrane, and may affect the structure of the FP when bound to membrane (52). Although there has not been any systematic study of the effect of cholesterol on the structure of SARS FPs, cholesterol is known to alter the structure of the HIV FP significantly as well as having an effect on the membranes (10,53).

## Why is FP-$Ca^{2+}$ interaction important for membrane fusion?

Calcium ions are important modulators of membrane fusion. Because of their positive charges, they possess a generally enhancing effect on membrane fusion by electrostatic interactions with negatively charged headgroups of lipid bilayers. They thus decrease the electrostatic repulsion of two opposing membranes that are in close proximity prior to undergoing fusion. Calcium ions can also directly interact with fusion protein machineries, thereby activating their fusogenicity; and in such cases membrane fusion is clearly calcium dependent. An example is the cellular SNARE-mediated synaptic vesicle fusion machinery (54–56) (i.e., without calcium ions present, membrane fusion does not take place). There are other situations in which calcium cations have been shown to interact with protein fusogens and enhance their fusogenicity; but without calcium, membrane fusion can still occur, albeit at a much reduced rate. In such cases membrane fusion is only partly dependent on calcium ions. The SARS-1, SARS-2 (16), and MERS FPs (15) are in this category.

$Ca^{2+}$ promotes the folding of SARS-1 FP in the membrane. First, from the CD spectra (Fig. 4 *A*), we can see an increase of helical content when the concentration of $Ca^{2+}$ increases. Second, the FP-membrane titration results (Fig. 7 *A* and *B*) showing that in the presence of $Ca^{2+}$, the FP folds better in the membrane. At the same time, $Ca^{2+}$ also promotes the ordering activity of FP in the $Ca^{2+}$ response experiment (Fig. 4 *B* and *C*). Thus, the binding of $Ca^{2+}$, the folding of FP in membranes, and the membrane ordering activity are strongly correlated.

In order to promote the folding of FP and the ordering activity of FP, a bound $Ca^{2+}$ ion needs to simultaneously bind to at least two binding sites. As we can see in the $Ca^{2+}$-FP titration (Fig. 6), even double mutants either in FP1 or FP2 have an N close to 2 (i.e., there is only a single negatively charged residue remaining in either the FP1 or FP2 segment), yet this residue can still bind one $Ca^{2+}$. However, as shown by the ESR, all double mutants basically have a very small ordering activity, about the same as that of triple mutants (Figs. 2 *C* and *D*, 3 *C* and *D*). This indicates that at least two $Ca^{2+}$ binding sites in each segment are required in order to maintain its "$Ca^{2+}$-enhanced" ordering activity.

Thus, it seems that $Ca^{2+}$ functions in two ways. The first is to fix the FP in the interfacial region of the bilayer to help the formation of secondary structure of the FP in membrane. The second is to promote the formation of tertiary structure of FP by holding two binding sites together. Both help the FP to insert into the membrane and thus induce the ordering effect (squeeze water molecules out of the headgroup region).

Previously (10), we found that the full-length SARS-1 FP (also known as FP1_2) induces a greater membrane ordering effect than the sum of the combined individual FP1 and FP2. FP1_2's ordering effect also reaches into the middle hydrophobic region (10PC), while neither FP1 nor FP2 has this ability. We have proposed that there is a synergistic effect because of the cooperation between the FP1 and FP2. Although the details of this cooperation are unknown, we suspect there is an FP1-FP2 interaction. As we have shown previously for the case of influenza HA, the interaction between FP-TMD increases its ability to perturb the membrane to a greater extent (11). Our research on HIV FPs also suggests that when HIV FPs are in an aggregate form, they induce a greater degree of membrane ordering and also the effect reaches deeper (10).

The recent NMR paper on SARS-2 FP structure mentioned above indicates that the FP inserts in the membrane as a wedge (23). In that model, FP1 is mainly a long helix (referred to as H1 in that paper), and the FP2 is composed of two short helices (referred to as H2 and H3 in that paper) linked by a flexible loop; and the FP1 (H1) and FP2 (H3) are positioned closely in membranes. Although that result applies to the SARS-2 FP, it is very reasonable that the SARS-1 FP would adopt a similar structure on the basis of the similarity between the SARS-1 and SARS-2 FPs. And although we argue above that the $Ca^{2+}$ binding topology in that study is different from ours, especially because of the lipid composition, it suggests the possibility of interaction(s) between FP1 and FP2.

A limitation of the present NMR and molecular dynamics simulation studies is that there is only one FP in their system: one FP in bicelles in the NMR study (23) or one FP in a membrane patch in the molecular dynamics simulations (36). These environments exclude the possibility of intermolecular interactions between the FPs. However, this can exist in our ESR study, as the FPs bind to liposomal membranes, which are large enough to harbor multiple FPs.

Considering the "real biological scenario," the three FPs are closely located in the whole S protein trimer. Thus, the FPs are likely to form trimers as well in solution or fluid membranes. It is even possible that a higher number N-mer can be formed if multiple S protein trimers accumulate near a fusion site. It has been shown that in the case of influenza, seven to nine trimers accumulate in the fusion site (57,58). HIV FPs are known to aggregate in the membrane and are expected to aggregate in the context of the whole gp41 trimer during membrane fusion as well (59). However, we needed an experimental system that simulates the "real biological scenario." That is why we developed a PP-SUV system.

## Does each separate FP function in the same fashion as the trimer of FP on the whole S protein trimer?

It has long been questioned whether separate FPs function the same as in the whole protein. The first use of phospholipid spin labels in an intact lipid-enveloped virus with complete glycoproteins to detect structure of viral membrane (the *cis* membrane) can be traced back to mid-1970s (60). However, the study on effect of intact glycoproteins on the *trans* membrane (the opposite membrane in the membrane fusion process) is very limited, especially for the use of a noninfectious model such as our PP-SUV system shown in this paper. Our PP-SUV methodology monitors the membrane ordering induced by the preassembled S protein on the surface of the PP in real time. This provides several advantages. First, the FP is now a part of the entire protein. Second, the protein is preassembled, presumably in a trimer as suggested by cryoelectron microscopy (17). This allows the three FPs in the trimer to be located in close proximity, which is quite different from separate FP monomers. Third, the S protein trimers are now on a membrane of the enveloped particle, in which the spatial distribution is similar to that on the viral surface. This is a more "biological scenario" than the separate FP. In addition, by using time-resolved ESR, we can monitor the change of order parameter $S_0$ in real time, which allows us to study the kinetics of membrane ordering as well.

We have obtained some useful observations using this method. First, the FP on the PP induces membrane ordering of a magnitude equivalent to that of the separate FP (Fig. 9 *E*). This strongly suggests that the "final" effect of FP on the PP and separate FP are similar.

Second, the mutations of the negatively charged residue affect both the extent and the kinetics of the ordering effect (Fig. 9 *D*), but the extent of the PP-induced ordering effect is similar to that of the corresponding separate FP. This confirms most results of our mutation study on the FP can be translated into the context of PP. The production of mutant S protein on PP is more difficult to control, as some mutants have very low expression levels or do not process well for complicated reasons. Thus, studies on FP mutants are still useful.

Third, the ordering activity of the whole protein is even more dependent on $Ca^{2+}$, as the "basal ordering activity" is minimal compared with that of the separate FPs (Fig. 9 *C*). But it is also possible that the "basal ordering activity" will require a longer time to take effect, which is beyond our current acquisition time range. We need more experiments to test this hypothesis.

Fourth and most relevant to our previous discussion of the intermolecular interaction, in an initial experiment, we found that the individual FPs induce membrane ordering to a similar extent, but much more slowly (Fig. 9 F). Although careful control of relative quantities is required, it appears that the PP is more rapid in inducing the local ordering. A likely reason is that trimers must first form from the individual FPs. This would strongly suggest the need for FP trimers and its benefit for membrane fusion. The FPs in the S protein on the PP is preassembled as a trimer, just like those on natural viral membranes. Thus, the initial trimerization of the FP leads to the local ordering effect. We suggest the possibility of an intermolecular FP1-FP2 interaction (i.e., the FP1 of one FP interacts with the FP2 of another FP). This would allow the FP1 and FP2 to cooperate to induce stronger and deeper ordering, as discussed above. It will require more studies to confirm this hypothesis.

Although we are still improving our methodology, it has already shown potential for studying the initial stage of membrane fusion. In particular, we can monitor in real

time how local membrane ordering develops in the SUV as mediated by the FPs in the complete glycoprotein trimers that are assembled on the PP surface. By comparing the kinetics of membrane ordering effects mediated by both the individual FP and the FP in the whole glycoprotein on PP membranes, we can expect to better understand this step in viral membrane fusion. In addition to studying the mechanism, this system is also able to serve as a platform for testing the effects of environmental factors (pH, ions, etc.) and the inhibitory effects of drugs, peptides, and antibodies that target the FP.

Although the present work is focused mainly on the SARS-1 FP, it is also useful for SARS-2 FP, as their sequences are similar. We show the ESR results of two SARS-2 mutants as examples in Fig. 8. Those mutants exhibit reduced ordering activity, as do the corresponding mutants for SARS-1 FP. We also show initial results for the SARS-2 PP-SUV (Fig. 9 *C*), and it is clear that the they are very similar to our results for SARS-1. Of course, as we have shown previously, although the SARS-2 and SARS-1 FPs differ only in three residues, the SARS-2 FP does have a significantly greater ordering effect (16).

### A model of SARS FP in membranes

A proposed model for the SARS-1 FP, on the basis of our observations and measurements, is shown in Fig. 10 *B* for an FP monomer. The bipartite FP or "platform" consists of two distinct subdomains, FP1 and FP2, each binding to a calcium ion via three negatively charged residues: aspartic acids (D) and glutamic acids (E). In the FP1 segment, D812 serves as a binding site, and the E801 and D802 serve together as another binding site and they are redundant; in the FP2 segment, E821, D825, and D831 serve as three binding sites. The loss of binding sites (i.e., by mutation) reduces its activity, especially when only one binding site is present. These $Ca^{2+}$ bindings promote the folding of the FP in the membrane and enable the FP to insert more deeply into the shallower hydrophobic region (5PC). This insertion leads to the dehydration of the membrane and results in the membrane ordering. The likely trimerization of FPs (we draw this trimer model separately in Fig. 10 *C*, omitting the $Ca^{2+}$ binding details as shown in Fig. 10 *B* for simplicity) enables cooperation of the FP1 and FP2 from adjacent FP units. This interaction is likely based on a helix-helix interaction. We have not observed a major beta strand structure in the CD, while the beta strand can be observed in the case of HIV FP using the same technique (53). The "wedge" model of the NMR study also suggests that FP1 and FP2 (of a monomer) are close in position in helical forms. The trimerization enables the FP to induce membrane ordering to a greater extent and deeper into the middle hydrophobic region (e.g., 10PC).

## SUPPORTING MATERIAL

Supporting material can be found online at https://doi.org/10.1016/j.bpj.2021.12.024.

## ACKNOWLEDGMENTS

This work was funded by NIH grants R01GM123779 and P41GM103521. We thank Tiffany Tang and Miya Kristine Bidon from the Dr. Susan Daniel lab and the Dr. Gary Whittaker lab for preparing the PP, examining the expression level, and measuring the concentrations. Dr. Daniel and Dr. Whittaker provided numerous helpful discussions and suggestions. We thank Dr. Brian Crane for the use of the CD spectrometer.

## REFERENCES

1. de Wit, E., N. van Doremalen, …, V. J. Munster. 2016. SARS and MERS: recent insights into emerging coronaviruses. *Nat. Rev. Microbiol.* 14:523–534.
2. Epand, R. M. 2000. Membrane fusion. *Biosci. Rep.* 20:435–441.
3. Blumenthal, R., M. J. Clague, …, R. M. Epand. 2003. Membrane fusion. *Chem. Rev.* 103:53–69.
4. Weissenhorn, W., A. Dessen, …, D. C. Wiley. 1999. Structural basis for membrane fusion by enveloped viruses. *Mol. Membr. Biol.* 16:3–9.
5. Tang, T., M. Bidon, …, S. Daniel. 2020. Coronavirus membrane fusion mechanism offers a potential target for antiviral development. *Antivir. Res.* 178:104792.
6. White, J., J. Kartenbeck, and A. Helenius. 1982. Membrane fusion activity of influenza virus. *Embo J.* 1:217–222.
7. Sieczkarski, S. B., and G. R. Whittaker. 2002. Dissecting virus entry via endocytosis. *J. Gen. Virol.* 83:1535–1545.
8. Ge, M., and J. H. Freed. 2009. Fusion peptide from influenza hemagglutinin increases membrane surface order: an electron-spin resonance study. *Biophys. J.* 96:4925–4934.
9. Ge, M., and J. H. Freed. 2011. Two conserved residues are important for inducing highly ordered membrane domains by the transmembrane domain of influenza hemagglutinin. *Biophys. J.* 100:90–97.
10. Lai, A. L., and J. H. Freed. 2014. HIV gp41 fusion peptide increases membrane ordering in a cholesterol-dependent fashion. *Biophys. J.* 106:172–181.
11. Lai, A. L., and J. H. Freed. 2015. Interaction between the influenza HA fusion peptide and transmembrane domain affects membrane structure. *Biophys. J.* 109:1–14.
12. Lai, A. L., J. K. Millet, …, G. R. Whittaker. 2017. The SARS-CoV fusion peptide forms an extended bipartite fusion platform that perturbs membrane order in a calcium-dependent manner. *J. Mol. Biol.* 429:3875–3892.
13. Nathan, L., A. L. Lai, …, S. Daniel. 2020. Calcium ions directly interact with the ebola virus fusion peptide to promote structure–function changes that enhance infection. *ACS Infect. Dis.* 6:250–260.
14. Pinello, J. F., A. L. Lai, …, T. G. Clark. 2017. Structure-function studies link class II viral fusogens with the ancestral gamete fusion protein HAP2. *Curr. Biol.* 27:651–660.
15. Straus, M. R., T. Tang, …, G. R. Whittaker. 2020. Ca 2+ ions promote fusion of Middle East respiratory syndrome coronavirus with host cells and increase infectivity. *J. Virol.* 94:e00426-20.
16. Lai, A. L., and J. H. Freed. 2021. SARS-CoV-2 fusion peptide has a greater membrane perturbating effect than SARS-CoV with highly specific dependence on Ca2+. *J. Mol. Biol.* https://doi.org/10.1016/j.jmb.2021.166946.
17. Gui, M., W. Song, …, X. Wang. 2017. Cryo-electron microscopy structures of the SARS-CoV spike glycoprotein reveal a

prerequisite conformational state for receptor binding. *Cell Res.* 27:119–129.

18. Walls, A. C., Y. J. Park, …, D. Veesler. 2020. Structure, function, and antigenicity of the SARS-CoV-2 spike glycoprotein. *Cell.* 181:281–292.e6.
19. Wrapp, D., N. Wang, …, J. S. McLellan. 2020. Cryo-EM structure of the 2019-nCoV spike in the prefusion conformation. *Science* https://doi.org/10.1126/science.aax0902.
20. Cai, Y., J. Zhang, …, B. Chen. 2020. Distinct conformational states of SARS-CoV-2 spike protein. *Science* https://doi.org/10.1126/science.abd4251.
21. Xia, S., M. Liu, …, L. Lu. 2020. Inhibition of SARS-CoV-2 (previously 2019-nCoV) infection by a highly potent pan-coronavirus fusion inhibitor targeting its spike protein that harbors a high capacity to mediate membrane fusion. *Cell Res.* 30:343–355.
22. Wang, Q., Y. Zhang, …, J. Qi. 2020. Structural and functional basis of SARS-CoV-2 entry by using human ACE2. *Cell* https://doi.org/10.1016/j.cell.2020.03.045.
23. Koppisetti, R. K., Y. G. Fulcher, and S. R. Van Doren. 2021. Fusion peptide of SARS-CoV-2 spike rearranges into a wedge inserted in bilayered micelles. *J. Am. Chem. Soc.* https://doi.org/10.1021/jacs.1c05435.
24. Georgieva, E. R., T. F. Ramlall, …, D. Eliezer. 2010. The lipid-binding domain of wild type and mutant α-synuclein: compactness and interconversion between the broken and extended helix forms. *J. Biol. Chem.* 285:28261–28274.
25. Georgieva, E. R., S. Xiao, …, D. Eliezer. 2014. Tau binds to lipid membrane surfaces via short amphipathic helices located in its microtubule-binding repeats. *Biophys. J.* 107:1441–1452.
26. Snead, D., A. L. Lai, …, D. Eliezer. 2017. Unique structural features of membrane-bound C-terminal domain motifs modulate complexin inhibitory function. *Front. Mol. Neurosci.* 10:1–17.
27. Madu, I. G., S. L. Roth, …, G. R. Whittaker. 2009. Characterization of a highly conserved domain within the severe acute respiratory syndrome coronavirus spike protein S2 domain with characteristics of a viral fusion peptide. *J. Virol.* 83:7411–7421.
28. Lai, A. L., H. Park, …, L. K. Tamm. 2006. Fusion peptide of influenza hemagglutinin requires a fixed angle boomerang structure for activity. *J. Biol. Chem.* 281:5760–5770.
29. Louis-Jeune, C., M. A. Andrade-Navarro, and C. Perez-Iratxeta. 2012. Prediction of protein secondary structure from circular dichroism using theoretically derived spectra. *Proteins.* 80:374–381.
30. Budil, D. E., S. Lee, …, J. H. Freed. 1996. Nonlinear-least-squares analysis of slow-motion EPR spectra in one and two dimensions using a modified Levenberg-Marquardt algorithm. *J. Magn. Reson. Ser. A.* 120:155–189.
31. Ge, M., D. E. Budil, and J. H. Freed. 1994. ESR studies of spin-labeled membranes aligned by isopotential spin-dry ultracentrifugation: lipid-protein interactions. *Biophys. J.* 67:2326–2344.
32. Ge, M., K. A. Field, …, J. H. Freed. 1999. Electron spin resonance characterization of liquid ordered phase of detergent-resistant membranes from RBL-2H3 cells. *Biophys. J.* 77:925–933.
33. Ge, M., A. Gidwant, …, J. H. Freed. 2003. Ordered and disordered phases coexist in plasma membrane vesicles of RBL-2H3 mast cells. An ESR study. *Biophys. J.* 85:1278–1288.
34. Millet, J. K., and G. R. Whittaker. 2016. Murine leukemia virus (MLV)-based coronavirus spike-pseudotyped particle production and infection. *Bio Protoc.* 6:e2035.
35. Ge, M., D. E. Budil, and J. H. Freed. 1994. An electron spin resonance study of interactions between phosphatidylcholine and phosphatidylserine in oriented membranes. *Biophys. J.* 66:1515–1521.
36. Khelashvili, G., A. Plante, …, H. Weinstein. 2021. Ca2+-dependent mechanism of membrane insertion and destabilization by the SARS-CoV-2 fusion peptide. *Biophys. J.* https://doi.org/10.1101/2020.12.03.410472.
37. Lou, Y., M. Ge, and J. Freed. 2001. A multifrequency ESR study of the complex dynamics of membranes. *J. Phys. Chem. B.* 105:11053–11056.
38. Ge, M., and J. H. Freed. 2003. Hydration, structure, and molecular interactions in the headgroup region of dioleoylphosphatidylcholine bilayers: an electron spin resonance study. *Biophys. J.* 85:4023–4040.
39. van Meer, G., D. R. Voelker, and G. W. Feigenson. 2008. Membrane lipids: where they are and how they behave. *Nat. Rev. Mol. Cell Biol.* 9:112–124.
40. Lai, A. L., L. K. Tamm, …, D. S. Cafiso. 2011. Synaptotagmin 1 modulates lipid acyl chain order in lipid bilayers by demixing phosphatidylserine. *J. Biol. Chem.* 286:25291–25300.
41. Takamori, S., M. Holt, …, R. Jahn. 2006. Molecular anatomy of a trafficking organelle. *Cell.* 127:831–846.
42. Frazier, A. A., C. R. Roller, …, D. S. Cafiso. 2003. Membrane-bound orientation and position of the synaptotagmin I C2A domain by site-directed spin labeling. *Biochemistry.* 42:96–105.
43. Patel, A., B.-P. Mohl, and P. Roy. 2016. Entry of bluetongue virus capsid requires the late endosome-specific lipid lysobisphosphatidic acid. *J. Biol. Chem.* 291:12408–12419.
44. Matos, P. M., M. Marin, …, G. B. Melikyan. 2013. Anionic lipids are required for vesicular stomatitis virus G protein-mediated single particle fusion with supported lipid bilayers. *J. Biol. Chem.* 288:12416–12425.
45. Zaitseva, E., E. Zaitsev, …, L. V. Chernomordik. 2017. Fusion stage of HIV-1 entry depends on virus-induced cell surface exposure of phosphatidylserine. *Cell Host Microbe.* 22:99–110.e7.
46. Hu, Y., and S. Patel. 2016. Thermodynamics of cell-penetrating HIV1 TAT peptide insertion into PC/PS/CHOL model bilayers through transmembrane pores: the roles of cholesterol and anionic lipids. *Soft Matter.* 12:6716–6727.
47. Yang, R., M. Prorok, …, D. P. Weliky. 2004. A trimeric HIV-1 fusion peptide construct which does not self-associate in aqueous solution and which has 15-fold higher membrane fusion rate. *J. Am. Chem. Soc.* 126:14722–14723.
48. Brennan, S. C., W. J. Wilkinson, …, D. Riccardi. 2016. The extracellular calcium-sensing receptor regulates human fetal lung development via CFTR. *Sci. Rep.* 6:21975.
49. Seelig, J., S. Nebel, …, C. Bruns. 1993. Electrostatic and nonpolar peptide-membrane interactions - lipid-binding and functional-properties of somatostatin analogs of charge Z = +1 to Z = +3. *Biochemistry.* 32:9714–9721.
50. Li, Y., X. Han, and L. K. Tamm. 2003. Thermodynamics of fusion peptide-membrane interactions. *Biochemistry.* 42:7245–7251.
51. Lai, A. L., and J. H. Freed. 2014. Influenza fusion peptide and transmembrane domain interaction induces distinct domains in lipid bilayers. *Biophys. J.* 106:707a.
52. Zakany, F., T. Kovacs, …, Z. Varga. 2020. Direct and indirect cholesterol effects on membrane proteins with special focus on potassium channels. *Biochim. Biophys. Acta Mol. Cell Biol. Lipids.* 1865:158706.
53. Lai, A. L., A. E. Moorthy, …, L. K. Tamm. 2012. Fusion activity of HIV gp41 fusion domain is related to its secondary structure and depth of membrane insertion in a cholesterol-dependent fashion. *J. Mol. Biol.* 418:3–15.
54. Bhalla, A., M. C. Chicka, …, E. R. Chapman. 2006. Ca(2+)-synaptotagmin directly regulates t-SNARE function during reconstituted membrane fusion. *Nat. Struct. Mol. Biol.* 13:323–330.
55. Brunger, A. T. 2005. Structure and function of SNARE and SNARE-interacting proteins. *Q. Rev. Biophys.* 38:1–47.
56. Chicka, M. C., E. Hui, …, E. R. Chapman. 2008. Synaptotagmin arrests the SNARE complex before triggering fast, efficient membrane fusion in response to Ca2+. *Nat. Struct. Mol. Biol.* 15:827–835.
57. Podbilewicz, B. 2014. Virus and cell fusion mechanisms. *Annu. Rev. Cell Dev. Biol.* 30:111–139.

58. Bentz, J., and A. Mittal. 2003. Architecture of the influenza hemagglutinin membrane fusion site. *Biochim. Biophys. Acta.* 1614:24–35.

59. Qiang, W., M. L. Bodner, and D. P. Weliky. 2008. Solid-state NMR spectroscopy of human immunodeficiency virus fusion peptides associated with host-cell-like membranes: 2D correlation spectra and distance measurements support a fully extended conformation and models for specific antiparallel strand regis. *J. Am. Chem. Soc.* 130:5459–5471.

60. Sefton, B. M., and B. J. Gaffney. 1974. Effect of the viral proteins on the fluidity of the membrane lipids in Sindbis virus. *J. Mol. Biol.* 90:343–358.